Received: 16 June 2022 | Revised: 6 October 2022 | Accepted: 18 October 2022

IET Generation, Transmission & Distribution

DOI: 10.1049/gtd2.12653

The Institution of Engineering and Technology WILEY

ORIGINAL RESEARCH

Distributed utility-based real-time power flow optimization in ICT-enabled low voltage distribution grids

Hanko Ipach[1] | Leonard Fisser[2] | Christian Becker[1] | Andreas Timm-Giel[2]

[1]Hamburg University of Technology, Institute of Electrical Power and Energy Technology (ieet), Hamburg, Germany

[2]Hamburg University of Technology, Institute of Communication Networks (ComNets), Hamburg, Germany

Correspondence
Hanko Ipach, Hamburg University of Technology, Institute of Electrical Power and Energy Technology (ieet), D-21079 Hamburg, Germany.
Email: hanko.ipach@tuhh.de

Funding information
Deutsche Forschungsgemeinschaft, Grant/Award Number: 426655646

Abstract

Low-Voltage (LV) distribution grids are facing a rapid increase of connected Photovoltaic (PV) power plants as well as flexible consumers like Battery-Electric Vehicle (BEV) chargers and Heat Pumps (HPs). The coordinated operation of these generation, storage and consumption units, referred to as Distributed Energy Resources (DERs), is regarded as a key requirement to maximize the benefits of renewable generation without violating, for example, voltage limits. Therefore, an operation management scheme was proposed in previous work that optimizes the power flows in LV grids in real-time, where optimality is expressed as a maximization of the utility that DER owners experience from power consumption or injection, respectively. In this contribution, this method is extended by: (1) detailing a time-varying utility-model to express customer needs, (2) introducing a distributed implementation enhancing the robustness to failures, (3) developing a testbed using a real-time digital power grid simulator and a communication network emulator, and (4) integrating a real-time information flooding protocol. The performance is evaluated in different simulation scenarios, showing that the proposed method is able to cooperatively utilize the flexible units in order to fulfil the DER owners' needs even in the event of controller failures and constrained communication.

1 | INTRODUCTION

As a result of the electricity supplies' transition towards climate-neutrality, renewable energy generators substitute conventional power plants. Not only is the source of energy changed in this process, but also the structure of electricity generation: while a rather small amount of large-scale power plants sufficed to supply the electricity demand in the past, many spatially distributed small-scale generators will have to jointly fulfill this task in the future electric power systems. At the same time, the decarbonization efforts in the mobility and residential heating sector are based largely on electrification: Battery-Electric Vehicles (BEVs) replace gasoline-fuelled cars, and Heat Pumps (HPs) are preferred over gas or oil heatings. These developments significantly change the role of Low-Voltage (LV) distribution grids within large power systems, which have traditionally been operated passively without monitoring and control. In view of the large peak voltage and power fluctuations that occur in LV grids with a high penetration of PV plants, EV chargers, and HPs, monitoring of the grid state and coordinated control of the flexible resources promises an alternative to cost-intensive grid expansions [1]. Furthermore, the coordinated operation of Distributed Energy Resources (DERs), which include both generation and flexible demand units here, offers the potential to adapt the flexible demand to the fluctuating supply from renewables and thus reduce the need to run costly, fossil-fuelled back-up power plants [2, 3].

1.1 | Literature review

Exploring the flexibility of DERs in LV grids in order to fulfill certain goals, for example, generation cost minimization, can be formulated as an Optimal Power Flow (OPF) problem [4]. Recently, feedback-based real-time OPF methods have gained attraction, for example, due to their performance in dynamically changing environmental conditions and their ability to cope with model inaccuracies [5–16].

They utilize online feedback optimization (OFO) algorithms that generally drive a system towards an optimal operating point by means of incremental updates. In most approaches proposed in literature, constraints on endogenous variables (e.g., node voltages) are incorporated based on direct measurements of the respective variables [5, 6, 8–12, 15, 16]. Hence, these approaches require to measure all endogenous quantities that are constrained in the OPF problem.

To take constraints on unmeasured quantities into account, OFO has been combined with State Estimation (SE) methods in [7, 13, 14]. While a weighted-least-squares (WLS) estimator is employed in [13], Kalman-filter-based approaches are utilized in [7, 14]. All three papers assume a central implementation with a dedicated controller for SE and OFO. In neither of the above, the communication network characteristics are explicitly considered. Furthermore, generic cost functions are utilized that do not incorporate any time-dependencies which might be introduced, for example, from user behavior.

In our previous work [17], we propose a real-time method for the coordinated control of DERs within a LV grid. It combines a branch-current based SE method and an OFO algorithm. Instead of minimizing a generic cost function as in [7, 14], a *utility* measure is introduced in [17] that should be maximized. The utility measure is inspired by optimization approaches from communication networks [18, 19], and in this context it is intended to quantify a DER's need for power consumption or generation. Each DER's utility is expressed by a generic, quadratic function of its active power consumption or generation and multiplied by an individual *priority*. Thus, by maximizing the sum of all DERs utility values, a fair and requirement-oriented allocation of the limited grid capacity among the DERs is achieved. The responsiveness of this approach increased robustness against DER failure as well as rapidly fluctuating power generation from Photovoltaic (PV) power plants. In simulations, the proposed operation management scheme successfully maximized the utility while respecting the voltage and current limits of the grid.

However, we identified some shortcomings of the method proposed in [17] with regard to the utility model. First, the model scope of DERs is limited to BEV and PV devices each with continuous power set points. Secondly, explicit rules to determine the priorities are missing, and finally, the power flow through the Medium-Voltage (MV)/LV transformer is not taken into account - hence, it is not possible to include, for example, power availability from MV connected wind power plants in the optimization. Furthermore, a centralized approach such as the one proposed in [17] introduces single-point-of-failures with respect to the controller entity and the required communication network infrastructure.

1.2 | Research gaps and contributions

Concluding from the above, we deem that a research gap exists with regard to distributed OPF approaches combining OFO and SE. Further research need concerns the joint in-depth modelling and testing of OFO based OPF and communication network behavior, which is especially relevant in distributed approaches with high communication demand, and the further development of the utility-based approach.

This work addresses this research need by building on [17]. First, we extend the optimization problem formulation and the solution algorithm. Specifically, DER type specific rules are detailed for BEVs and HPs to dynamically set their priority depending on their operational state, and DERs with switching behavior and minimum switch-on powers are incorporated. Also, we assign a utility function to the power flow across the MV/LV substation transformer. By varying the substation utility and/or the power limits over time, the availability of power in the superordinate MV grid can be taken into account in the optimization. This additional input allows to reflect the fluctuating power infeed from renewable power generation in the MV grid, for example, wind turbines. Second, the optimization process is moved from a centralized implementation to a distributed one, in which so-called Intelligent Node Controllers (INCs) located at each prosumer jointly solve the online optimization problem. This shift replaces the central management entity by multiple independent optimization agents, increasing robustness and resilience against node failures. The distributed approach is characterized by a periodic measurement broadcast between all INCs, such that each INC is able to perform a SE to compute the LV grid state. Similar to the control algorithm, the Information and Communications Technology (ICT) is re-organized as well. Instead of a cellular network architecture using base stations, nodes can communicate and exchange the required information directly. The extensive capacity and latency requirements for online optimization on the communication network are addressed by introducing an efficient and appropriate data dissemination protocol. To verify the proposed distributed optimization, a co-emulation testbed combining grid and communication network emulation is set up. In this testbed, the electrical LV grid is simulated on a Real Time Digital Simulator (RTDS) which emulates the grid, the prosumer and DER models. The INC as well as the communication network connecting them are emulated on a separate server allowing for an evaluation under realistic computational constraints.

The scientific contributions of this work can be summarized by:

1. We propose a distributed utility-based online power flow optimization relying on ICT-enabled smart prosumers and LV grid SE.
2. The associated communication network challenges are solved by integrating a real-time information flooding protocol.
3. The optimization framework allows formulating time-varying constraints on the substation transformer power flow to track superimposed renewable generation in the superordinate MV grid.
4. We evaluate the proposed management scheme in a real-time grid simulation and communication network emulation.

The proposed optimizing control method can be interpreted as a cooperative and service-oriented approach in electrical power supply. Instead of focusing on momentary active power, prosumers are interested in getting the service they need: for example, a charged EV battery upon departure or a consistently heated home. The INCs intend to autonomously utilize the available power and energy supply, which can differ considerably throughout the day, to fulfill these services, such that prosumers do not have to worry about the fluctuating supply.

1.3 | Structure of the paper

The paper is organized as follows. In Section 2, we present the LV grid and DER modelling. This sets the stage for the proposed distributed control approach, which is then detailed in Section 3. Afterwards, a description of the co-emulation testbed is given in Section 4. Section 5 details the data dissemination protocol, its performance in simulation and the model used to integrate characteristic communication network behavior into the emulation platform. Finally, Sections 6 and 7 discuss the distributed control approach's performance in a LV test grid under normal 24-h operation and operation under node-failure or communication network degradation, respectively. Section 8 concludes this work by summarizing the outcomes and putting the results into context for future research.

2 | LOW VOLTAGE GRID MODELLING

This section describes the LV grid model with residential load as well as PV power plants, BEV chargers and HPs.

2.1 | Grid model

We consider a LV grid with a single connection to the superordinate MV grid by means of an MV/LV substation transformer. The LV grid is of the three-phase four-wire type and has a radial structure, which is typical for German LV distribution grids [20]. As single phase loads introduce voltage and current imbalances, it explicitly considers the three phases, whereas the neutral conductor is incorporated using the Kron reduction technique (assuming neutral grounding) [21]. The transformer connection group is Dyn. Distribution lines can be overhead lines or underground cables.

The grid topology is described by the set of nodes $\mathcal{N}$ and the set of branches $\mathcal{B}$, where each branch $b \in \mathcal{B}$ connects two nodes. Without loss of generality, we consecutively number the grid nodes, with 0 being the transformer MV terminal. While shunt capacitance are neglected due to the short branch lengths, inductive phase coupling is considered. Thus, a LV branch is modelled by an impedance matrix $Z \in \mathbb{C}^{3\times3}$. We further denote the vector of phase-to-ground voltage phasors at node n by $\boldsymbol{v}_n = (v_{n,a}, v_{n,b}, v_{n,c})^\top \in \mathbb{C}^3$ and the vector of current phasors of branch b (connecting nodes n and m) by $\boldsymbol{i}_b = (i_{b,a}, i_{b,b}, i_{b,c})^\top \in \mathbb{C}^3$. Thus, the voltage drop across branch b is

$$\boldsymbol{v}_m - \boldsymbol{v}_n = Z \cdot \boldsymbol{i}_b. \tag{1}$$

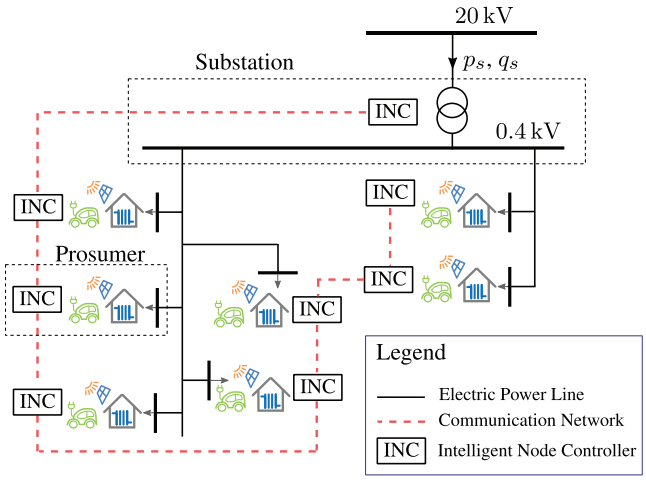

FIGURE 1 Schematic diagram of a LV grid with prosumers

Utilizing the short-circuit equivalent circuit diagram for the transformer, an analogous equation describes the transformer voltage drop.

Nodes where loads and/or generators are connected to the grid are called *prosumer nodes*, with the set of prosumer nodes $\mathcal{N}_\mathcal{P} \subset \mathcal{N}$. A prosumer node $n_r \in \mathcal{N}_\mathcal{P}$ injects a net active power $\boldsymbol{p}_{n_r} \in \mathbb{R}^3$ and a net reactive power $\boldsymbol{q}_{n_r} \in \mathbb{R}^3$ into the grid. Note that knowledge of the voltage phasor $\boldsymbol{v}_0 \in \mathbb{C}^3$ and all prosumers' net injected powers allows to compute the grid state, which is typically expressed in terms of the node voltage phasors $\{\boldsymbol{v}_n | n \in \mathcal{N}\}$, by means of a power flow calculation. In case of missing data, substitute values (e.g. from historic data) are required to perform the power flow calculation. When further data is available, for example, from actual measurements, State Estimation methods are applicable [22]. A schematic LV grid diagram is shown in Figure 1.

2.2 | Prosumers

We assume that one *prosumer* is located at each prosumer node and denote the set of prosumers by $\mathcal{P}$. Each prosumer $r \in \mathcal{P}$ at least contains a time-varying, possibly unbalanced inflexible load $\boldsymbol{p}_{r,\text{fix}}$ and $\boldsymbol{q}_{r,\text{fix}}$ that cannot be influenced by external control signals. The inflexible load summarizes the residential electricity demand of household appliances. Additionally, a prosumer optionally owns DERs that provide a certain flexibility regarding their power generation or consumption. A metering device measures the net injected active and reactive power $\boldsymbol{p}_r \in \mathbb{R}^3$ and $\boldsymbol{q}_r \in \mathbb{R}^3$ as well as the voltage $\boldsymbol{v}_r \in \mathbb{C}^3$ at the prosumer node. According to the most relevant types of DERs in residential grids, we specifically model HPs, BEVs and PV plants. These are described in the following subsections. The prosumer configuration is depicted in Figure 2.

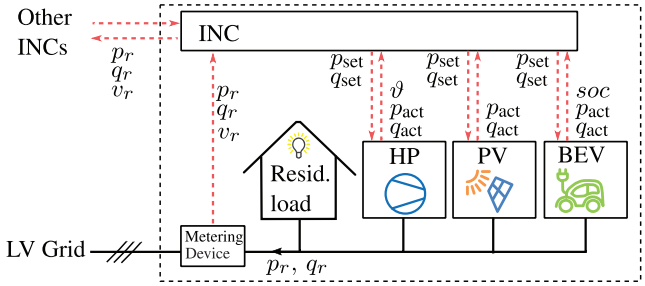

FIGURE 2 Prosumer configuration and process data exchange with the INC

2.2.1 | Photovoltaic power plants

We consider PV plants that consist of solar panels and an inverter for grid connection. The solar panels provide active power to the inverter, and their capability is specified by the plant's peak power p_{peak}. The peak power p_{peak} denotes the electrical power supplied by the panels at a solar irradiance of $G_{\text{ideal}} = 1000\text{W m}^{-2}$ without considering temperature dependent degradation. In operation, the solar irradiance G_{panel} on the panels varies and thus the maximum active power

$$p_{\max} = \frac{G_{\text{panel}}}{G_{\text{ideal}}} \cdot p_{\text{peak}}, \tag{2}$$

the PV panels can provide. To compute the solar irradiance on tilted PV panels from irradiance measurement data, we utilize the model proposed in [23]. It is extended by a temperature dependent degradation according to [24]. Furthermore, the model assumes that a Maximum Power Point Tracker (MPPT) tracker constantly adjusts the panel voltage such that the panels deliver the maximum power in varying environmental conditions.

We model the PV plant as a three-phase power source that is able to inject balanced active and reactive power into the grid up to its apparent power rating s_{n}. While the active power is limited by $p_{\max}$, the apparent power is limited by s_{n}. Within the limits, both active and reactive power can be adjusted by external setpoints p_{set} and q_{set}. In case the apparent power limit is exceeded, the inverter reduces p_{set} and q_{set} in equal shares, thus keeping the intended power factor. The inverter and MPPT dynamics are modelled as a single PT1 element with a time constant of 1s.

2.2.2 | Battery electric vehicles

According to common charger ratings, we consider either single phase electric vehicle chargers with a nominal power of $p_{\text{n}} = 3.7\text{kW}$ or three-phase chargers with ratings of either $p_{\text{n}} = 11\text{kW}$ or $p_{\text{n}} = 22\text{kW}$. Deviating from today's standard, the chargers support bidirectional charging, that is, they can discharge the battery to inject power into the grid. The active power is continuously adjustable in the range between maximum discharging and maximum charging power, and a constant efficiency η is assumed for both charging and discharging. The maximum charging and discharging power depends on the battery's State of Charge (SoC): at $20\% \leq soc \leq 80\%$, charging and discharging with nominal power is possible. Below 20%, discharging is prohibited, and above 80%, the maximum charging power decreases exponentially. When the SoC reaches a limit of 90%, charging is stopped. The battery is assumed to have a constant capacity E_{bat}, that is, self-discharging or aging effects are neglected. The dynamics of the charger are modelled as a PT1 element. In contrast to the PV plants, the BEV charger inverters operate at a constant power factor and only allow adjustment of the active power.

2.2.3 | Heat pumps

Due to the plurality of variants arising from, for example, various possible heat sources, different hot water usage options and hydraulic circuit designs, the modelling of HPs is challenging. The approach followed here aims at a compromise between a simple model on one hand and a sufficiently accurate model of the flexibility regarding the electric power consumption on the other hand.

We model the secondary hydraulic circuit of a HP as a water storage tank of a certain volume V, which is modelled as a constant heat capacitance $C_p = c_p \cdot \rho \cdot V$ with a variable (but homogenous) temperature ϑ, where $c_p = 0.4\text{kJkg}^{-1}\text{K}^{-1}$ is the specific heat capacitance of water and its density is $\rho = 1\text{kgL}^{-1}$. The storage is cooled down by the outward-pointing heat flow $\dot{Q}_{\text{out}} = \dot{Q}_{\text{cons}} + \dot{Q}_{\text{loss}}$ corresponding to the prosumer's heat demand $\dot{Q}_{\text{cons}}$ on one hand and heat losses $\dot{Q}_{\text{loss}}$ on the other hand. The heat losses are proportional to the difference between the water temperature ϑ and the ambient air temperature ϑ_{amb} around the storage, so

$$\dot{Q}_{\text{loss}} = k_l \cdot A \cdot (\vartheta - \vartheta_{\text{amb}}), \tag{3}$$

where $k_l = 0.6\text{Wm}^{-2}\text{K}^{-1}$ is a heat-transfer coefficient and A is the tank surface. Note that A is calculated assuming a cylindrical tank with volume V and a radius-to-height ratio of $\frac{r}{h} = 0.23$ [25].

The method to derive the electrical HP power is largely based on [26]. The heat demand $\dot{Q}_{\text{cons}}$ during a specific day is derived as follows: first, a normalized Standard Load Profile (SLP) is chosen according to the building type and the mean temperature on the target day. Then, it is scaled according to the prosumer's daily heat demand, which is derived from the annual heat demand and a correction factor depending on the temperature at the target day. This results in a time series of the required heat flow during the target day.

The water storage is heated up by an inward heat flow $\dot{Q}_{\text{in}}$ during heat pump operation, such that

$$\dot{Q}_{\text{in}} - \dot{Q}_{\text{out}} = C_p \cdot \frac{\text{d}}{\text{dt}}\vartheta. \tag{4}$$

It is calculated by multiplying the electrical pump power p_{el} by the Coefficient of Performance (COP), which depends on the temperature difference between heat source and heat sink:

$$\dot{Q}_{in} = \mathrm{cop}(\vartheta_{source}, \vartheta_{sink}) \cdot p_{el}. \quad (5)$$

This dependency is modelled by the COP curves presented in [26]. Whereas the water storage is assumed to be the heat sink, different heat sources can be defined, namely air, brine, and groundwater. Thus, their respective temperature is required to accurately determine the COP. Depending on the availability of data, we utilize actual measurements or estimations. On the electrical side, the HP is modelled as a modulating pump. Therefore, the electric power consumption in on-state is variable within a range defined by a minimum power $p_{min,on}$ and a maximum power p_{max}. Furthermore, it is assumed to be balanced and three-phase. The inverter dynamics are modelled as a PT1 element, and the pump is assumed to operate at a fixed power factor.

An additional heating rod is not foreseen. Commonly, it is installed in heat pump systems to provide a back-up supply when the heating power of the pump is too low due to, for example, extreme environmental conditions. Assuming that the pump is well dimensioned to cover the heat demand even in unfavorable conditions, we omit the (rather inefficient) heating rod operation.

Several constraints are assumed during operation that limit the available flexibility. First, minimum delays for transitions between on- and off-state are considered to prevent frequent switching events. Furthermore, minimum and maximum water temperatures ϑ_{min} and ϑ_{max} can be defined for the heat storage. If the water temperature increases above the upper threshold, the pump is forced to switch off. Likewise, it is switched on when the temperature decreases below the lower limit. Finally, the maximum power threshold is limited when the water temperature approaches its upper limit.

3 | DISTRIBUTED REAL-TIME POWER FLOW OPTIMIZATION

This section details the real-time power flow optimization method we propose to operate LV grids with a high share of DERs as modelled in Section 2, where prosumers are connected by a communication network. As a start, Section 3.1 contains a discussion of the qualitative objectives. Then, the concept to accomplish these objectives is presented in Section 3.2 in terms of the distributed controller architecture and the data exchange. Afterwards, detailed explanations are provided in Section 3.3 on the utility model, which constitutes the objective function that our control approach aims to maximize, and on the online algorithm employed to solve the optimization problem in Section 3.4.

3.1 | Objectives

The main objective of our approach is to utilize the fluctuating electricity supply that is expected in LV grids within electric power systems relying mainly on wind and solar power plants in a way that maximizes the benefit for the prosumers within the LV grid. In addition to the LV grid situation, varying superordinate grid's preferences should be taken into account. In this way, the renewable generation in the superordinate grid should be considered (notably, self-sufficiency of the LV grid is not necessarily a target). Furthermore, stationary constraints on the voltage level at each node within the LV grid are to be complied with. This also applies to thermal limit currents of the substation transformer and the distribution lines.

Beyond that, the implementation of the control method should ensure flexibility and robustness: adding or removing DERs of different types or prosumers should be facilitated, and failures of individual controllers or communication links should impair the control performance as little as possible. Also, in view of the high variety of individual DERs, the dependency on accurate DER models should be little. Furthermore, a convenient approach with little requirements on manual user input is strived for, thus enabling a high degree of autonomy in the LV grid operation.

3.2 | Distributed real-time utility maximization concept

To pursue the above objectives, we propose a distributed real-time utility maximization based on our previous work [17]. One key aspect is the quantification of a DER's benefit from a certain power consumption or injection by means of a concave utility function that maps active power p to a utility value ϕ. In contrast to [17], such a utility is also formulated here for the power flow across the substation transformer, which is also referred to as *substation power* in the remainder of this work. Furthermore, strict power limits are applied to the substation power as well. The control objective is thus the maximization of the sum of all DERs' and the substation transformer's utilities under the voltage and current magnitude constraints imposed by the grid, the substation power limits and operational limits of the DERs.

In the distributed approach proposed here, this task is jointly carried out by INCs located at each prosumer node and at the MV/LV substation, which are all connected by a communication network. Each prosumer INC is in charge of taking measurements of the voltage as well as the active and reactive power flow at its grid connection point, as depicted in Figure 2, whereas the substation INC collects power flow measurements at the LV feeders. These measurements are broadcast among the INCs.

On the basis of the measurements and an electrical model of the grid, each INC performs a SE to obtain estimations of the phase-to-ground voltage phasors at all grid nodes and the

three-phase current phasors on all grid branches. The INCs employ the same SE algorithm as in [17], which has been proposed in [27]. It is tailored to unbalanced and three-phase grids. The concept proposed here, however, could also be applied to single-phase grids if the SE was replaced by a single-phase method. The SE provides each INC with sufficient data to perform one incremental optimization step, that is, every prosumer INC then computes an incremental update of the active and reactive power setpoints for the DERs assigned to it.

It should be noted that in each timestep, the utility maximization is formulated as a quasistatic optimization problem. However, the optimization problem changes over time due to, for example, time-varying utility functions, changing inflexible loads and fluctuating solar irradiation. Therefore, an important issue is how well the incremental algorithm can "track" the dynamics of the optimization problem formulation.

At this stage the utility functions have not been mathematically formulated, and it is unclear how the incremental update towards the utility maximization is derived. These issues are tackled in the following subsections. First, the utility computation is detailed in Section 3.3. Afterwards, the update step is explained in Section 3.4.

3.3 | Utility functions

The idea behind the utility functions is to quantify the benefit that DERs experience when they consume or inject a certain power from or into the LV grid, respectively. The utility approach differs from classical OPF approaches that usually aim at a minimization of generation costs. As proposed in [17], each DER's utility function is composed of two parts: a basic utility function Φ_{base} and a priority factor w, resulting in the utility

$$\Phi_c = w_c \cdot \Phi_{\text{base},c}, \forall c \in \mathcal{C}, \tag{6}$$

where $\mathcal{C}$ denotes the set of all DERs in the LV grid. The basic utility function has the same structure for all DERs. It is explained in Section 3.3.1. The priority factor depends on the DER state and user input data. Extending the approach in [17], we propose concrete functions to determine the priority of the DER types considered here based on the DER models presented in Section 2. These are explained in Section 3.3.2. The substation utility function, which is also newly introduced here, is detailed in Section 3.3.3.

3.3.1 | Basic utility functions

The basic utility function maps a DER's active power to its utility value. It is defined by

$$\Phi_{base,c}(p_c(t)) = |p_{\text{n},c}| \cdot \left(1 - \left(\frac{p_c(t) - p_{\text{n},c}}{p_{\text{n},c}}\right)^2\right) \quad \forall c \in \mathcal{C}, \tag{7}$$

where $p_{\text{n},c}$ denotes the nominal active power of DER c ($p_{\text{n}} = p_{\max}$ for HPs and $p_{\text{n}} = p_{\text{peak}}$ for PV plants), and $p_c(t)$ its active power injection at time t. Note that both nominal and momentary active power are signed: positive values denote generators and power injection into the grid, and negative values are used for consumers and power consumption, respectively.

The basic utility function has some important properties. First, a DER's utility is zero when its momentary power injection is zero, and it reaches its maximum when the power injection equals the nominal power. This implies that each generator or consumer wants to maximize its power injection or consumption, respectively, up to its nominal value. Second, the marginal utility $\frac{\mathrm{d}\Phi_{\text{base},c}}{\mathrm{d}p_c}$, that is, the utility gain from an incremental power increase, is zero at nominal power and linearly increases in magnitude with rising distance from the nominal power. Therefore, for an exemplary consumer, an increase of power consumption is rated more valuable when the actual consumption is low compared to when it is close to its nominal value. A utility maximizing algorithm is thus supposed to favor an even distribution of the available power, which is expected to result in a certain fairness among the DERs.

3.3.2 | Priority factors

The basic utility functions only consider the momentary active power of a DER, and their shape is static. Hence, they do not allow to take individual prosumer preferences or DER states, which might differ over time, into consideration. This implies that energy related aspects are ignored by the basic utility functions, though they presumably relate to the user experience much closer than the momentary power (e.g. a BEV owner is not so much interested in the actual charging power, but rather in the battery's SoC).

As a solution, we introduce priority factors that are utilized to scale the basic utility functions. A high priority factor signifies an urgency of power consumption or injection, depending on whether a consumer or producer is considered. The priority factor w_c of a DER c is generally a function of its state $\boldsymbol{x}_c$ and user input data $\boldsymbol{u}_c$, where $\boldsymbol{x}_c$ and $\boldsymbol{u}_c$ depend on the type of c. While specific functions to compute w for BEV and HPs are proposed below, other implementations are imaginable, which meet certain requirements:

- The priority factor is bounded on a fixed interval,
- and it slowly changes with time.

While the first requirement ensures that the utility remains bounded and the fairness aspect is kept (i.e. the maximum priority is the same for all DERs), the second requirement ascertains that the utility maximization problem at a certain time t is quasi-static, that is, the time dependency of the priority factors does not have to be taken into account in the optimization algorithm design.

Referring to the DER models introduced in Section 2, the PV plants get constant unity priority factors, such that no PV plant

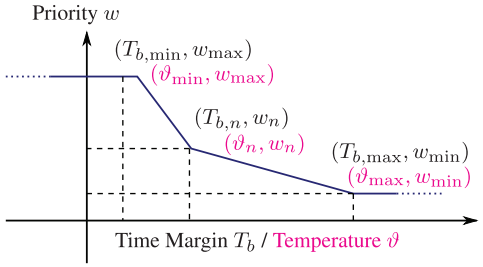

FIGURE 3 Priority functions for BEVs (black) and HPs (magenta)

is discriminated in case a power curtailment is necessary. On the contrary, dynamic priority factors are proposed for BEVs and HPs as detailed below.

Battery electric vehicles: Upon arrival at the charging station, a BEV owner inputs the next scheduled departure time t_{dep} and a target state of charge soc_{target}. Based on the battery capacity E_{bat}, the nominal charging power p_{n}, the charging efficiency η_{ch} and the actual state of charge $soc(t)$, the minimum charging duration required to reach the target SoC is

$$T_{\text{ch,min}}(t) = \frac{(soc_{\text{target}} - soc(t)) \cdot E_{\text{bat}}}{p_{\text{n}} \cdot \eta_{\text{ch}}}. \tag{8}$$

The time margin

$$T_b(t) = t_{\text{dep}} - t - T_{\text{ch,min}}(t), \tag{9}$$

then denotes the maximum time the charger could wait until it would have to start charging at maximum power to reach the SoC target. We utilize it as a measure to quantify the urgency of power consumption: the smaller T_b, the higher the need to consume charging power to meet the owner's target. According to this dependency, we model a BEV's priority factor as a piecewise linear function of T_b. It is characterized by three sample points, and the resulting function is shown in Figure 3.

It can be seen that within $T_{b,\min}$ and $T_{b,\max}$, the priority factor is linearly interpolated between the sampling points. Outside this interval, it is fixed at $w_{\max}$ (for $T_b(t) < T_{b,\min}$) or $w_{\min}$ (for $T_b(t) > T_{b,\max}$).

Heat pumps: For HPs, we use similar piecewise linear functions to determine the priority factors. Again, three sample points are specified using $w_{\min}$, w_n and $w_{\max}$, and the priority factor is interpolated, as shown in Figure 3. The heat storage temperature $\vartheta(t)$ serves as a measure to quantify the urgency of power consumption. For technical and user comfort reasons, it is assumed to be restricted to a certain interval $[\vartheta_{\min}, \vartheta_{\max}]$. Generally, the higher ϑ, the lower the need of power consumption. Thus, w takes its specified minimum value when ϑ reaches its defined upper limit. Likewise, w is maximal when the heat storage temperature is at the defined lower threshold.

It should be emphasized that even though we use the DER models from Section 2 to define the priority functions, real time feedback based approaches like the one proposed here are generally robust to model errors [5]. To a certain extent, real-time measurements of the relevant DER states substitute accurate model information. For example, the actual transfer function mapping electrical heat pump power to heat storage temperature is not required to be known, but instead temperature measurement values have to be accessible for the INC to compute the priority factor.

3.3.3 | Substation utility function

The substation utility function should express the preference of the superordinate MV grid to inject power into the LV grid or draw power from the LV grid, respectively. This preference is assumed to be time-varying due to, for example, fluctuating infeed from wind turbines: in times of high wind power, there could be a power surplus in the MV grid, so a power transfer to the LV grid would be desired. On the other hand, when the power output from wind turbines is low, a power shortage in the MV grid would result in a preference to draw power from the LV grid.

We assign concave quadratic utility functions Φ_s^p and Φ_s^q similar to the DER utility function to the substation power p_s and reactive power q_s, respectively. In contrast to the DER functions, the power value corresponding to the maximum utility is time-varying, instead of fixing the apex at the nominal power like in (7). This allows to express the above-mentioned varying preference. Additionally, for numerical stability reasons, an upper limit $\gamma_{\max}$ restricts the marginal utility, that is, the first derivative of Φ_s^p with respect to p_s. The resulting utility function for active power reads

$$\Phi_s^p(p_s(t)) = \begin{cases} \gamma_{\max} \cdot (p_s(t) - \check{p}_s) + \check{\Phi}_s^p, & p_s(t) < \check{p}_s \\ -\frac{1}{2} w_s^p \cdot (p_s(t) - p_{s,t})^2 + \Phi_{s,0}^p, & \check{p}_s \le p_s(t) \le \hat{p}_s, \\ -\gamma_{\max} \cdot (p_s(t) - \hat{p}_s) + \hat{\Phi}_s^p, & p_s(t) > \hat{p}_s \end{cases} \tag{10}$$

where

$$\check{p}_s = -\frac{\gamma_{\max}}{w_s^p} + p_{s,t}, \qquad \hat{p}_s = \frac{\gamma_{\max}}{w_s^p} + p_{s,t},$$
$$\check{\Phi}_s^p = \hat{\Phi}_s^p = -\frac{\gamma_{\max}^2}{2 w_s^p} + \Phi_{s,0}^p, \tag{11}$$

and w_s^p denotes a constant weighting factor. The maximum utility value $\Phi_{s,0}^p$ is a constant parameter. The substation active power utility function is sketched in Figure 4.

An analogous utility function is applied to the reactive power flow. Thus, by means of the target reactive power $q_{s,t}$, the MV grid can express a desire to exchange a certain reactive power with the LV grid, for example, for voltage support.

In contrast to the DER output power, the substation active and reactive power flows p_s and q_s cannot be controlled directly. Instead, they result from the power injected and consumed by

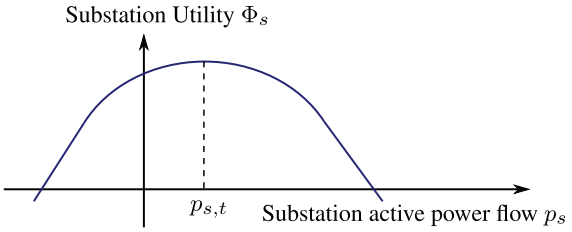

FIGURE 4 Substation utility function. The target power flow $p_{s,t}$ varies according to the MV grid preference

the LV grid's prosumers, which can be formulated as

$$p_s(t) = -\sum_{r\in\mathcal{P}} p_r(t) + p_{\text{loss}}(t)$$
$$= -\sum_{r\in\mathcal{P}}\left(\sum_{c_r\in\mathcal{C}_r} p_{c_r}(t) + p_{r,\text{fix}}(t)\right) + p_{\text{loss}}(t), \quad (12)$$

where p_{loss} denotes the grid losses and $\mathcal{C}_r$ the set of prosumer r's DERs. An equation analogous to (12) can be formulated for the reactive power flow q_s.

3.4 | Online utility maximization

This section presents the optimization problem formulation, the online algorithm employed for its solution, and the distributed implementation. Though the algorithm equals the one used in [17] to a certain extent, we provide a complete description here for better readability.

3.4.1 | Objective function

On the basis of the DER and substation utility functions introduced above, the overall utility maximization objective function reads

$$\Phi_{\text{tot}} = \sum_{c\in\mathcal{C}} \Phi_c(p_c) + \Phi_s^p(p_s) + \Phi_s^q(q_s). \quad (13)$$

It should be noted that (13) constitutes a dynamic objective function. The DER utility functions, for instance, depend on the DER states that vary with time. Likewise, the substation power flow not only depends on the control variables p_c, $q_c\ \forall c \in \mathcal{C}$, but also on the inflexible loads that change over time. Looking at the situation at a certain instant of time, however, (13) can be considered static. Then, it can be shown that neglecting the grid losses in (12), the objective function is concave.

3.4.2 | Constraints

Several constraints apply to the utility maximization problem. The first set of constraints refers to operational limits of the LV grid. Namely, node voltage and branch current magnitudes should remain within their pre-defined limits. We assume balanced operation of the grid, that is, equal load on all three phases, and thus apply limits to the positive sequence node voltages $v_n^+\ \forall n \in \mathcal{N}$ and branch currents $i_b^+\ \forall b \in \mathcal{B}$. Denoting $\underline{v} \in \mathbb{R}$ and $\overline{v} \in \mathbb{R}$ for lower and upper voltage limits, respectively, the node voltage constraints read

$$\underline{v} \le |v_n^+| \le \overline{v} \quad \forall n \in \mathcal{N}. \quad (14)$$

Writing $\overline{i}_b$ for the thermal limit current of branch b, the current constraints are formulated as

$$|i_b^+| \le \overline{i}_b \quad \forall b \in \mathcal{B}. \quad (15)$$

The second set of constraints reflects the operational limits of DERs. We generally assume that box constraints apply for active and reactive power of a DER, that is

$$p_c \in [\underline{p}_c, \overline{p}_c] \quad \forall c \in \mathcal{C}, \quad (16)$$

$$q_c \in [\underline{q}_c, \overline{q}_c] \quad \forall c \in \mathcal{C}. \quad (17)$$

Furthermore, an upper limit for the apparent power is considered to take, for example, inverter ratings into account, implying

$$s_c = \sqrt{p_c^2 + q_c^2} \le \overline{s}_c\ \forall c \in \mathcal{C}. \quad (18)$$

In contrast to the grid constraints (14) and (15), the DER operational limits are dynamic; for instance, the maximum power of a PV plant depends on the fluctuating solar irradiation.

The final set of constraints refers to the substation power. Lower and upper limits for both active power flow p_s and reactive power flow q_s across the transformer are defined, so

$$p_s \in [\underline{p}_s, \overline{p}_s], \quad (19)$$

$$q_s \in [\underline{q}_s, \overline{q}_s]. \quad (20)$$

3.4.3 | Primal-dual online algorithm

The overall optimization problem cast into a minimization problem reads

$$\min_{p_c, q_c, \forall c\in\mathcal{C}} -\Phi_{\text{tot}}$$
$$\text{s.t. } (14), (15), (16), (17), (18), (19), (20), \quad (21)$$

where Φ_{tot} is defined in (13).

As explained in the previous sections, both the objective function and the constraints are influenced by exogenous, uncontrollable inputs that are time-varying, for example, the solar irradiation. At a certain instant of time, however, (21)

constitutes a static optimization problem. It should be noted that the nonlinear power flow equations render (3.4.3) a non-convex optimization problem.

A classical feedforward optimization approach would solve (21) as a static problem on the basis of a model of the LV grid, DER power limits and measurements or estimations to quantify the impact of exogenous inputs. Such an approach comes with several drawbacks, for instance, model inaccuracies or inexact estimations of exogenous inputs can lead to a suboptimal or infeasible solution, and the computational complexity to solve (21) until convergence can be high for large grids. Therefore, we apply the online, feedback-based approach proposed in [17] which is based on [5]. It relies on a high update rate with a frequent collection of measurement data. Then, in each control cycle, only one incremental step is done towards the optimum. Therefore, the model dependency is reduced, changing environmental conditions are quickly captured, and the complexity is low.

The update rules are derived from applying a gradient dual ascent/ primal descent approach to the partial Lagrangian

$$\begin{aligned}\mathcal{L}(\boldsymbol{p}_c, \boldsymbol{q}_c, \boldsymbol{\lambda}_-.\boldsymbol{\lambda}_+, \boldsymbol{\mu}, \nu_-, \nu_+, \xi_-, \xi_+) \\ = -\Phi_{tot}(\boldsymbol{p}_c, \boldsymbol{q}_c) + \boldsymbol{\lambda}_-(\underline{\boldsymbol{v}} - |\boldsymbol{v}|) + \boldsymbol{\lambda}_+(|\boldsymbol{v}| - \overline{\boldsymbol{v}}) \\ + \boldsymbol{\mu}(|\boldsymbol{i}| - \overline{\boldsymbol{i}}) + \nu_-(\underline{p}_s - p_s) + \nu_+(p_s - \overline{p}_s) \\ + \xi_-(\underline{q}_s - q_s) + \xi_+(q_s - \overline{q}_s).\end{aligned} \tag{22}$$

of (21), where $\boldsymbol{\lambda}_-, \boldsymbol{\lambda}_+ \in \mathbb{R}^{|\mathcal{N}|}$ and $\boldsymbol{\mu} \in \mathbb{R}^{|\mathcal{B}|}$ are vectors of dual multipliers associated with the constraints (14) and (15), respectively, and $\nu_-, \nu_+, \xi_-, \xi_+ \in \mathbb{R}$ are dual multipliers referring to the substation power constraints (19) and (20). The update rules to solve the dual problem

$$\max_{\boldsymbol{\lambda}_-, \boldsymbol{\lambda}_+, \boldsymbol{\mu}, \nu_-, \nu_+, \xi_-, \xi_+} \left(\min_{\boldsymbol{p}_c, \boldsymbol{q}_c} \mathcal{L} \right), \tag{23}$$

can be separated into primal and dual updates. The dual updates at time instant $t_{k+1} = t_k + T_s$, where T_s is the cycle time of the algorithm, are

$$\boldsymbol{\lambda}_-(k+1) = \left[\boldsymbol{\lambda}_-(k) + \alpha_v \cdot (\underline{\boldsymbol{v}} - |\boldsymbol{v}(k)|)\right]_{\geq \mathbf{0}}, \tag{24}$$

$$\boldsymbol{\lambda}_+(k+1) = \left[\boldsymbol{\lambda}_+(k) + \alpha_v \cdot (|\boldsymbol{v}(k)| - \overline{\boldsymbol{v}})\right]_{\geq \mathbf{0}}, \tag{25}$$

$$\boldsymbol{\mu}_+(k+1) = \left[\boldsymbol{\mu}_+(k) + \alpha_i \cdot (|\boldsymbol{i}(k)| - \overline{\boldsymbol{i}})\right]_{\geq \mathbf{0}}, \tag{26}$$

$$\nu_-(k+1) = \left[\nu_-(k) + \alpha_p \cdot (\underline{p}_s - p_s)\right]_{\geq 0}, \tag{27}$$

$$\nu_+(k+1) = \left[\nu_+(k) + \alpha_p \cdot (p_s - \overline{p}_s)\right]_{\geq 0}, \tag{28}$$

$$\xi_-(k+1) = \left[\xi_-(k) + \alpha_q \cdot (\underline{q}_s - q_s)\right]_{\geq 0}, \tag{29}$$

$$\xi_+(k+1) = \left[\xi_+(k) + \alpha_q \cdot (q_s - \overline{q}_s)\right]_{\geq 0}, \tag{30}$$

where $[\cdot]_{\geq \mathbf{0}}$ denotes a component-wise projection onto the set of positive numbers and $\alpha_v, \alpha_i, \alpha_p, \alpha_q \in \mathbb{R}$ are stepsize parameters. The dual update rules (24)-(30) numerically integrate constraint violations.

The primal update rules read

$$\begin{aligned}\tilde{\boldsymbol{p}}_{\text{set}}(k+1) = \boldsymbol{p}(k) + \alpha\big(\nabla_{\boldsymbol{p}}\Phi_{\text{tot}}(k) \\ - S_{pv}^{\top}(k)\big(\boldsymbol{\lambda}_+(k+1) - \boldsymbol{\lambda}_-(k+1)\big) \\ - S_{pi}^{\top}(k)\boldsymbol{\mu}(k+1) \\ - s_{pp}\big(\nu_+(k+1) - \nu_-(k+1)\big)\big),\end{aligned} \tag{31}$$

$$\begin{aligned}\tilde{\boldsymbol{q}}_{\text{set}}(k+1) = \boldsymbol{q}(k) + \alpha\big(\nabla_{\boldsymbol{q}}\Phi_{\text{tot}}(k) \\ - S_{qv}^{\top}(k)\big(\boldsymbol{\lambda}_+(k+1) - \boldsymbol{\lambda}_-(k+1)\big) \\ - S_{qi}^{\top}(k)\boldsymbol{\mu}(k+1) \\ - s_{qq}\big(\xi_+(k+1) - \xi_-(k+1)\big)\big),\end{aligned} \tag{32}$$

where $\tilde{\boldsymbol{p}}_{\text{set}}, \tilde{\boldsymbol{q}}_{\text{set}} \in \mathbb{R}^{|C|}$ are vectors of power setpoints for all DERs, $\boldsymbol{p}, \boldsymbol{q} \in \mathbb{R}^{|C|}$ contain actual DER power values, $\alpha \in \mathbb{R}$ is a stepsize parameter, and $\nabla_{\boldsymbol{p}}\Phi_{\text{tot}}$ and $\nabla_{\boldsymbol{q}}\Phi_{\text{tot}}$ denote the gradients of Φ_{tot} with respect to $\boldsymbol{p}$ and $\boldsymbol{q}$, respectively. The matrices $S_{xy}, x \in \{p, q\}, y \in \{v, i\}$ are sensitivity matrices that provide linear mappings of nodal power changes (active and reactive) to node voltage and branch current magnitude changes. As explained in [17], they are derived from a linearization of the power flow equations at the estimated grid state according to the SE result. Furthermore, $s_{pp} \in \mathbb{R}$ and $s_{qq} \in \mathbb{R}$ denote sensitivity coefficients of p_s and q_s with respect to DER power values. Neglecting grid losses, $s_{pp} = s_{qq} = -1$ holds according to (12).

It should be noted that regularization terms have been added to the Langrangian in [5] to derive convergence claims for the online primal-dual algorithm. As in [17], these are omitted here as our numerical experiments indicate robust convergence even without regularization.

In case of constraint violations, the update rules (24)–(32) lead to an integral-type control response. To enhance the dynamic performance when substation power limits are violated, we add a proportional control gain according to

$$\begin{aligned}\acute{p}_{\text{set},c}(k+1) = \tilde{p}_{\text{set},c}(k+1) + \frac{1}{|C|}\big([p_s(k) - \overline{p}_s]_{\geq 0} \\ - [\underline{p}_s - p_s(k)]_{\geq 0}),\end{aligned} \tag{33}$$

$$\begin{aligned}\acute{q}_{\text{set},c}(k+1) = \tilde{q}_{\text{set},c}(k+1) + \frac{1}{|C|}\big([q_s(k) - \overline{q}_s]_{\geq 0} \\ - [\underline{q}_s - q_s(k)]_{\geq 0}) \quad \forall c \in \mathcal{C},\end{aligned} \tag{34}$$

where $\tilde{p}_{\text{set},c}$ and $\tilde{q}_{\text{set},c}$ denote the entries in $\tilde{\boldsymbol{p}}_{\text{set}}$ and $\tilde{\boldsymbol{q}}_{\text{set}}$ corresponding to DER c. Hence, (33) and (34) evenly distribute the power required to correct a limit violation among the DERs. Note that the proportional gains vanish asymptotically in case a feasible point is found by the primal-dual algorithm, because the dual approach enforces zero constraint violations

asymptotically. Here, we assume that the flexibility provided by the DERs is always sufficient to steer the LV grid into a feasible point.

Note that the DER output power constraints have not been considered in the setpoint computation yet. Therefore, the final DER set values $p_{\text{set},c}$ and $q_{\text{set},c}$ are obtained from projecting $\acute{p}_{\text{set},c}$ and $\acute{q}_{\text{set},c}$ onto their feasible range as defined in (16)-(17), resulting in

$$p_{\text{set},c}(k+1) = \left[\acute{p}_{\text{set},c}(k+1)\right]_{[\underline{p}_c, \bar{p}_c]} \quad \text{and} \tag{35}$$

$$q_{\text{set},c}(k+1) = \left[\acute{q}_{\text{set},c}(k+1)\right]_{[\underline{q}_c, \bar{q}_c]} \quad \forall c \in \mathcal{C}. \tag{36}$$

3.4.4 | Distributed implementation

In [17], a central controller was in charge of controlling all DERs within the LV grid and applied the above update rules. To avoid a single point of failure, we propose a distributed implementation here, where INCs are located at each prosumer in the grid, and the INCs jointly solve the utility maximization. In the distributed implementation, the INCs broadcast measurement data of nodal voltage as well as active and reactive nodal power values to all other INCs in each control cycle (see Figure 2). Thus, every INC is able to perform a LV grid state estimation and compute local versions of the dual updates (24)-(30). Furthermore, every INC computes the entries of the sensitivity matrices $S_{xy}, x \in \{p, q\}, y \in \{v, i\}$ that belong to its location within the grid.

Then, each INC determines $\acute{p}_{\text{set},c}$ and $\acute{p}_{\text{set},c}$ according to (31)-(34) that belong to its associated DERs. Besides the dual updates and the sensitivity matrices, the objective function's gradients $\nabla_{\boldsymbol{p}}\Phi_{\text{tot}}$ and $\nabla_{\boldsymbol{q}}\Phi_{\text{tot}}$ are needed to compute these primal updates. For a specific DER $c \in \mathcal{C}$, only the entries $\nabla_{p_c}\Phi_{\text{tot}}$ and $\nabla_{q_c}\Phi_{\text{tot}}$ are relevant. Utilizing (13), (10), (12), (6) and (7), we derive

$$\begin{aligned}
\nabla_{p_c}\Phi_{\text{tot}}(k) &= \nabla_{p_c}\left(\sum_{c\in\mathcal{C}} \Phi_c(p_c(k)) + \Phi_s^p(p_s(k)) + \Phi_s^q(q_s(k))\right) \\
&\approx \left.\frac{d\Phi_c}{dp_c}\right|_{p_c(k)} + \left.\frac{d\Phi_s^p}{dp_s}\right|_{p_s(k)} \cdot \frac{\partial p_s}{\partial p_c} \\
&= 2w_c|p_{\text{n},c}| \cdot \left(1 - \left(\frac{p_c(k) - p_{\text{n},c}}{p_{\text{n},c}}\right)\right) \\
&\quad + \left[2w_s^p \cdot (p_s(k) - p_{s,t})\right]_{[-\gamma_{\max},\gamma_{\max}]},
\end{aligned} \tag{37}$$

where $[\cdot]_{[-\gamma_{\max},\gamma_{\max}]}$ denotes projection onto $[-\gamma_{\max}, \gamma_{\max}]$, and active and reactive grid losses p_{loss} and q_{loss} have been neglected in the computation of the substation transformer power flow sensitivity with respect to nodal power changes, that is, $\frac{\partial p_s}{\partial p_c} = -1$ and $\frac{\partial q_s}{\partial p_c} = 0$. Given that line losses are usually a few percent of the line power flow, the error introduced by this gradient approximation is low.

In (37), $p_{\text{n},c}$ is the constant nominal DER power, $p_c(k)$ the actual DER power measured at time t_k and w_c the DER's priority factor. The latter is noted here as a constant, but it should be kept in mind that it depends on the DER state and therefore (slowly) varies with time. Furthermore, the substation active power priority factor w_s^p, the target substation active power $p_{s,t}$ and the marginal utility limit $\gamma_{\max}$ are substation parameters, of which $p_{s,t}$ is time-varying according to Section 3.3.3 (again, its dynamics are assumed slow compared to the cycle time T_s). Hence, updates of $p_{s,t}$ must be sent to the INCs on a regular basis. Finally, $p_s(k)$ is the active power flow across the substation as estimated by the SE at time t_k.

The primal update for the reactive power of a DER $c \in \mathcal{C}$ is derived accordingly, resulting in

$$\begin{aligned}
\nabla_{q_c}\Phi_{\text{tot}}(k) &= \nabla_{q_c}\left(\sum_{c\in\mathcal{C}} \Phi_c(p_c(k)) + \Phi_s^p(p_s(k)) + \Phi_s^q(q_s(k))\right) \\
&\approx 0 + 0 + \left.\frac{d\Phi_s^q}{dq_s}\right|_{q_s(k)} \cdot \frac{\partial q_s}{\partial q_c} \\
&= \left[2w_s^q \cdot (q_s(k) - q_{s,t})\right]_{[-\gamma_{\max},\gamma_{\max}]},
\end{aligned} \tag{38}$$

where $q_{s,t}$ is the target substation reactive power. Note that DER utility functions are only defined for active power, and analogously to (37), we assume $\nabla_{q_c}\Phi_s^p(p_s(k)) \approx 0$, neglecting the coupling between nodal reactive power and the substation active power. Therefore, only the last summand of the objective function (13) results in a non-zero value in (38).

The final step in the computation of power set points is the projection onto the set of feasible DER power values according to (35) and (36). The DERs do this projection themselves, meaning that in case $\acute{p}_{\text{set},c}$ or $\acute{q}_{\text{set},c}$ is infeasible, they adjust their active and reactive power to the closest feasible value. Thus, each control cycle of an INC at prosumer r ends with sending the set points $\acute{p}_{\text{set},c}$ and $\acute{q}_{\text{set},c}$, $c \in \mathcal{C}_r$ to the prosumer's DERs.

The optimization algorithm assumes that the DERs accept continuous power setpoints, which limits its applicability. To incorporate a DER c with a non-zero minimum power $p_{\min,\text{on},c}$ in switched-on mode, we follow a simple approach: in control cycle k, the INC stores the setpoint $\acute{p}_{c,\text{set}}(k)$. When in the next cycle $k+1$ either the measured actual power $p_c(k)$ or $\acute{p}_{\text{set},c}(k)$ are smaller than $p_{\min,\text{on},c}$, the INC replaces $p_c(k)$ by $\acute{p}_{\text{set},c}(k)$ in the primal update (31).

3.5 | Interim conclusion

This section ends with an interim conclusion on the distributed utility maximizing concept proposed above.

First, we address the proposed integration of the substation power into the optimization problem formulation by means of a utility function. In contrast to determining binding set values like proposed in, for example, [5], the utility function approach

leaves some freedom to the LV grid's DERs in regard to how close the target value is met. To illustrate this, assume that in a setting with constant exogenous inputs and constant DER states, the algorithm has reached an equilibrium without any constraints being active, that is, (14)–(20) hold true. Then, the first-order optimality conditions require $\nabla_{q_c}\Phi_{\text{tot}} = 0\ \forall c \in \mathcal{C}$. According to (31) with $\frac{\partial p_s}{\partial p_c} \approx -1$, this implies that

$$\left.\frac{d\Phi_c}{dp_c}\right|_{p_c(k)} \approx \left.\frac{d\Phi_s^p}{dp_s}\right|_{p_s(k)} \qquad \forall c \in \mathcal{C}, \tag{39}$$

that is, all DERs' marginal utilities approximately equal the substation's marginal utility. It is usually the case that the resulting common marginal utility is nonzero, so neither DERs nor substation are operating at their maximum utility. The algorithm result can then be interpreted as a compromise between DER and substation preferences. One benefit compared to the fixed set point approach is that integrator windup, which could occur for the fixed set point approach when it is incorporated in the same dual fashion as the other constraints, is not an issue.

As a result of the dualization of, for example, voltage and current constraints, integrator windup can occur when the DER flexibility does not suffice to reach a feasible point. As mentioned in Section 3.4.3, it is assumed that the active and reactive power flexibility provided by the DERs is always sufficient to steer the LVs grid into a feasible point where no voltage, current, or transformer power limits are violated. This limits the applicability to grids that cannot be overloaded by non-controllable loads or generators, which we deem is not a very strong assumption provided that all DERs participate in the control.

Another aspect worth discussing is the distributed concept we follow, with a measurement broadcast and a SE at each INC. Commonly, distributed approaches feature reduced computation and communication requirements, for example, only local communication between neighboring controllers. In comparison to these, the broadcast-based approach here with a full SE at each INC puts a higher burden on the communication network and the INC performance. We deem, however, that this drawback is outweighed by the benefit of having actual measurements rapidly available for grid SE at each INC. In a fully distributed SE with only local information passing among neighboring INCs, on the contrary, it takes many communication data exchanges until a changing state of a DER (or an effect thereof) is recognized at a distant node [15, 28]. Furthermore, LV grids cover limited areas that are supposedly well coverable by a communication network, and a limited number of nodes such that the complexity to perform a SE is bounded. Due to its importance in this context, the following sections elaborate on the communication network architecture proposed here to support the utility maximization in a realistic LV grid setting. A detailed analysis of the performance requirements for INCs, however, is out of the scope of this paper.

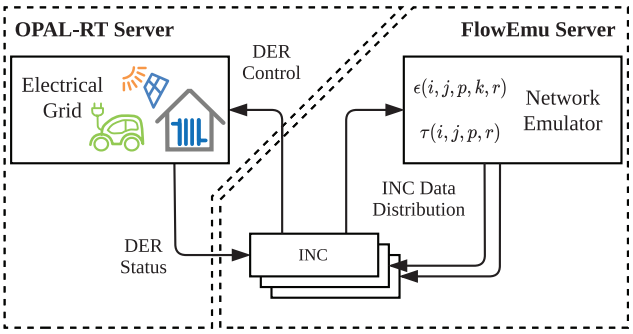

FIGURE 5 Co-Emulation platform combining grid simulation and communication network emulation

4 | CO-EMULATION PLATFORM

The proposed control method is to be evaluated under realistic communication network constraints. For this we develop a co-emulation platform which allows for Hardware in the Loop (HIL) grid simulations as well as real-time communication between INCs. The co-emulation platform is similar to the design proposed in [29], but offers substantially higher flexibility in electrical grid as well as communication network modeling. In contrast to the setup in [29], the electrical grid and communication network emulations take place on dedicated hardware and software instead of running jointly on shared servers. The testbed used for this work includes an electrical grid simulator, virtualized INC instances and a communication network emulator. Two separate servers are used to isolate the electrical grid from the virtualized controller instances and their associated communication network. A setup schematic is shown in Figure 5 and a brief description for each component is given in the following paragraphs.

4.1 | Electrical grid

We implement the LV grid model detailed in Section 2 in MATLAB® and Simulink® (Release R2019b) and deploy it on an OPAL-RT OP5707XG RTDS.

The components of the electrical power grid itself, that is, the MV/LV substation transformer and the LV cables, are simulated using the three-phase models explained in 2.1. Then, a self-written power flow calculation tool on the basis of a backward-forward-sweep procedure [30] solves the nonlinear three-phase power flow equations. In doing so, the transformer primary connections constitute the slack node where the voltage phasors are assumed constant, and all prosumer nodes are modelled as PQ nodes. This quasi-static approach yields a very efficient implementation with little computational complexity, thus enabling to simulate large grids. In case future applications require a more sophisticated simulation of the electric grid, the power flow calculation could be replaced, for example, by an Electro-Magnetic Transients (EMT) model using the Simscape™ Electrical™ toolboxes.

Prosumer models including residential load and DERs as described in Section 2.2 complete the LV grid model. These models generally read environmental data like solar irradiation or temperatures from pre-saved files containing time series data. Therefore, different environmental conditions can be applied without changing the model.

In the co-emulator setup, the INCs are not included in the LV grid model, but ruon an external server instead. The RTDS communicates with the external server via Ethernet. To send measurement data to and receive control input from its dedicated INC, the RTDS establishes a TCP/IP server socket for each prosumer.

4.2 | Intelligent node controllers

Intelligent Node Controllers represent the logical connection between electrical grid, DERs, and communication network. They are responsible for distributing local measurements to other nodes as well as calculating power set values for connected DERs. Each virtual INC instance is connected to its corresponding DERs (BEV, PV, HP) as well as its metering device (Smart Meter (SM)) running within the OPAL-RT grid simulation. The communication between the INC and its electrical counterparts is considered to be ideal, as these devices would be situated physically close to each other in a real world scenario. Periodic measurement updates supplied by the metering device have to be forwarded by each INC to all other INCs using the dissemination protocol introduced in Section 5.1. The communication between different INCs is established over the FlowEmu [31] network emulator. Each INC runs in an isolated Linux container and interfaces to the FlowEmu instance as well as its respective DERs running within the OPAL-RT Server through its dedicated UDP or TCP/IP stack using network namespaces. This virtualization allows for flexible setups and configuration of emulation environments without requiring extensive hardware setup.

4.3 | FlowEmu network emulator

Transmissions between INCs are subjected to communication network effects such as packet loss and delays. To introduce these characteristics, data being sent between INCs is first passed to the network emulator FlowEmu [31]. Packets are then delayed for a communication delay and dropped with a loss probability based on the specified ICT model. Finally, the packet is forwarded to all other INCs for which the packet was not dropped. A detailed description of the used communication network model is given in Section 5.2. The FlowEmu server is equipped with an AMD Ryzen 9 5950X 16-Core processor from which one core is reserved for the FlowEmu application and the remaining 15 cores are shared among the INC instances.

In contrast to the popular open-source network emulator NetEm [32] (also used in [29]), FlowEmu allows for fully customizable network models including packet dissection, manipulation, duplication, delay and dropping. Furthermore, INC instances running on additional hardware (either additional servers, or dedicated programmable logic controllers) can be directly integrated by the nature of emulation.

5 | INFORMATION AND COMMUNICATION TECHNOLOGY

Operation of future distribution grids will be heavily characterized by new and emerging smart grid applications such as Advanced Metering Infrastructure (AMI), Demand Response (DR) or Distributed Automation (DA) [33]. ICTs play a crucial role for deployment of such services by providing the necessary communication network. However, the requirements on delay, throughput, and reliability can vary significantly between applications. The degree of heterogeneity is further increased by looking at the capabilities of different ICTs [34]. For instance, while cellular networks excel in cost-efficiency by enabling long-range point-to-point communication, they introduce a single point of failure, the base station. This trade-off may make cellular networks suitable for applications such as AMI, while making it difficult to deploy in scenarios with critical DA. Selecting the appropriate ICT for specific applications and allowing multiple communication networks to coexist are therefore crucial steps towards a smart and future-oriented distribution grid.

The envisioned control method introduced in Section 3 requires global knowledge of electrical measurements at INCs during operation. Since INCs alone can only observe the local state of the grid, information has to be disseminated within the grid by a supporting communication network. The main recipient for the information shared by INCs are other INCs within the same LV distribution grid. Beyond the distribution grid's bounds, the information value decrease sharply and information may only be of interest to central entities such as a Distribution System Operator (DSO)'s control center. In fact, considering privacy and security risks as well as communication network capacity, limiting the extent of the dissemination as much as possible is desirable. To match the distributed and local nature of the control method, a communication network based on IEEE 802.11 is evaluated within the scope of this work. It has to be noted, that the communication network is solely used by the control method, and no background traffic is assumed. This assumption is inline with the idea of deploying different ICTs for different applications, as cellular networks may take over the job of serving other smart grid applications.

Section 5.1 introduces the data dissemination protocol used to support the proposed control method and Section 5.2 describes its integration into the emulation platform.

5.1 | Data dissemination protocol

This section details the data dissemination protocol which is required to enable the proposed control method. Each INC needs to disseminate its local voltage measurements and power set values to all other INCs, while simultaneously collecting measurements itself. From the communication network point of

view, this data exchange facilitates itself as an N-to-N broadcast problem. A generalized broadcast protocol has been introduced by the authors in [35] and is further adapted to fully support the control method presented in this paper.

Disseminating information from each node to all other nodes is a challenging task for distributed multi-hop networks, as $N(N-1)$ different source-destination flows have to be established. To address this, the whole dissemination process is organized sequentially and as such is multiplexed in time. INCs take turns disseminating their local information using a round-robin scheme, effectively turning the N-to-N broadcast problem into multiple, separate 1-to-N ones. After the successful and complete dissemination of a node's information, the subsequent node is allowed to transmit its data. Once the last node finishes its dissemination, the first node restarts the process.

This sequential approach allows for optimal dissemination of each individual information packet, as the whole network capacity is allocated exclusively to a single source-destination flow. In large networks, however, this limitation may result in low utilization because nodes idle wait for the next information packet. To address this, multiple source-destination flows can be disseminated simultaneously at the cost of sharing network capacity. This trade-off was analyzed in depth in [35] and since the network considered in this work only consists of relatively few nodes, we limit our evaluation to pure sequential flooding.

A Virtual Backbone Network (VBN) is used to organize individual disseminations. The VBN is established using a Minimum Connected Dominating Set (MCDS) [36] policy and a subset of nodes is promoted to the role of backbone nodes. Data dissemination using a MCDS reduces the maximum number of hops required to reach all nodes in the network. The full flooding process is characterized by two main phases. In the first phase, the data itself is distributed. A node's data is transmitted to its associated backbone node and then propagated throughout the network along the VBN. Each backbone node ensures that all of its associated leaf nodes as well as its neighboring backbone nodes successfully receive the data. Although the data is now fully distributed, the sequential nature of the flooding process necessitates a second signaling phase. In the second phase, the backbone nodes of the VBN have to determine that the current dissemination is finished and trigger the start of the next one.

An overview about the different packet types necessary is given in Table 1.

In addition to the seven packet types formulated in the original paper [35], the protocol is further extended for the evaluation of this work. Two additional packet types (*SKIP*, *RECONNECT*) are introduced to allow for nodes to leave and re-join the sequential flooding process. Table 1 also features short-identifiers for each packet type which are used in the exemplary dissemination process depicted in Figure 6.

The network consists of four leaf $\{L_1, L_2, L_3, L_4\}$ and three backbone $\{B_1, B_2, B_3\}$ nodes. Edge labels suggest a transmission order and denote the respective packet type. The dissemination starts with node L_1 transmitting its data to its associated backbone node B_1 (*D1*). B_1 then forwards the data to its associated leaf node L_3 and neighboring backbone node B_2 (*BD2*).

TABLE 1 Data dissemination protocol packet types

Identifier	Description
D	Data transmission from a leaf node to its backbone node.
D-ACK	Acknowledgement for a *D* transmission.
BD	DATA relay by a backbone node to its leaf nodes and VBN.
BD-ACK	Acknowledgement for *BD*
S	Indication of backbone node's successful dissemination.
S-ACK	Acknowledgement for *S*.
NR	Requesting the transmission of a new update.
SKIP	Signaling to bypass a node's data dissemination.
RECONNECT	Integrator states for optimizer reinitialisation.

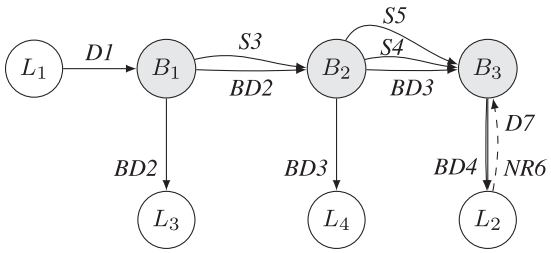

FIGURE 6 Dissemination process of information from L_1. Acknowledgements for point-to-point reliability have been left out for visibility. Edge labels indicate packet type

The same data forwarding occurs at the other backbone nodes $\{B_2, B_3\}$. Once all leaf nodes of backbone node B_1 acknowledged the successful reception of the data, the backbone node B_1 can confirm its successful dissemination towards the backbone node which is responsible for the next node in sequence (*S3*). In this example the next node would be L_2 and its associated backbone node B_3. As the acknowledgement from node B_1 arrives at node B_2 (*S3*), it needs to be further relayed to the correct backbone node (*S4*). The same acknowledging occurs at the other backbone nodes (*S5*). Once the backbone node responsible for the next node receives acknowledgements from all backbone nodes, a new data request can be sent (*NR6*). Leaf node L_2 answers promptly with a new data packet to be disseminated (*D7*). The same dissemination process then repeats for the data of node L_2.

The example highlights how data and signaling packets propagate through the network but omits the additional acknowledgements required to ensure full reliability. Data transmissions between backbone nodes and leaf nodes are secured using additional data acknowledgements (*BD-ACK*, *D-ACK*). Furthermore, signaling packets and their relay transmissions are implicitly acknowledged by broadcast overhearing, if this fails a dedicated *S-ACK* acknowledgement is sent.

Finally, the purpose of the two additional packet types (*SKIP*, *RECONNECT*) are elaborated. Disconnected nodes (identified by repeatedly missing *BD-ACK*) have to be skipped so that the flooding process does not preempt. The dissemination

of a missing node's packet is bypassed by sending *SKIP* packets from its associated backbone node to the next node. This process is similar to the signaling process established by *S* and *S-ACK* packets, but without the prior condition on full dissemination. Once an INC reconnects and start to acknowledge data transmissions again, the backbone transmits a special *RECONNECT* packet. The packet contains necessary information to reinitialize the INC's optimizer states, that is, the dual variables $\boldsymbol{\lambda}_-, \boldsymbol{\lambda}_+, \boldsymbol{\mu}, \nu_-, \nu_+, \xi_-, \xi_+$ (see Section 3.4.3).

5.2 | Information and Communications Technology model

We use an IEEE 802.11-based network to establish communication between INCs. This means that transmissions take place on a wireless medium experiencing Media Access Control (MAC) delays as well as packet loss due to collisions. For the FlowEmu network emulator to replicate these characteristics within the co-emulation framework, stochastic descriptions for packet loss and delay are required. Numerical values were derived using network simulations using the SimPy framework [37]. A unit-disk channel model was assumed for which the communication range of all nodes were set to the smallest value which still ensures a connected network. Retransmission timeouts were set to 40 ms and ten repetitions each covering 360 s of simulation time were conducted.

5.2.1 | Packet loss

The packet loss model describes the connectivity of INCs. Packet loss is detected by the absence of acknowledgements from the receivers and triggers a retransmission after a specified timeout. As the retransmission timeout has to be at least twice as large as the packet delay (to allow for a full round-trip), even a single packet loss can significantly slow down the dissemination process. A sophisticated packet loss model is therefore crucial for accurate ICT emulation.

The packet loss is differentiated with respect to five dimensions. First, the loss probability is dependent on the physical locations of transmitter i and receiver j. Nodes out of communication range experience critical packet loss and cannot communicate at all. Second, loss probabilities vary significantly depending on the packet type p being transmitted. An initial data transmission by a leaf node experiences no contention on the wireless medium by nature of the dissemination protocol (see Section 5.1). In contrast, a signaling packet being forwarded to a backbone node may find the node busy transmitting a data packet to its respective leaf nodes. Furthermore, the packet loss depends on the payload k being disseminated. Due to differences in the payload length and the starting position of the dissemination process, congestion on the wireless medium may differ. The final dimension of packet loss is the retransmission stage s. Retransmissions generally experience less contention, as node activity decreases with time due to the progress of the dissemination. The packet loss ϵ is therefore described by

$$\epsilon(i, j, p, k, s) \quad \forall(\{i, j, k\} \in N, p \in P, s \in S), \tag{40}$$

where N is the number of nodes, P is the number of packet types, and S is the maximum retransmission stage.

5.2.2 | Delay

The delay model describes the node-to-node delay a transmission experiences. The model focuses on the main delays found in wireless sensor networks and includes the propagation delay t_{prop}, the transmission delay t_{trans} and the media access delay t_{mac}.

For the propagation delay a transmitter i and destination j tuple (i, j) is used to calculate the propagation delays defined by the wave propagation

$$t_{\text{prop}}(i, j) = \frac{d(i, j)}{c}, \tag{41}$$

where $d(i, j)$ is the physical distance between two nodes and c is the speed of light.

The transmission delay t_{trans} is independent of the source-destination-tuple and is defined as

$$t_{\text{trans}}(p) = \frac{N_{bit}(p)}{R}, \tag{42}$$

where $N_{bit}(p)$ is the packet size of packet type p and R is the wireless medium data rate.

Finally, the tuple (i, p, s) describes the different medium access delays used for packets of type p transmitted by node i at retransmission stage s. In contrast to the previously described delays, the medium access delay $t_{\text{mac}}(i, p, s)$ is not a constant. Instead, random samples for $t_{\text{mac}}(i, p, s)$ are drawn from the stochastic process $f_{(i,p,s)}$.

The total delay for a packet of type p to be transmitted from node i to node j at retransmission stage s is found as

$$\tau(i, j, p, s) = t_{\text{prop}}(i, j) + t_{\text{trans}}(p) + t_{\text{mac}}(i, p, s). \tag{43}$$

Table 2 shows an excerpt of simulation results for a backbone (Node 31) and a leaf node (Node 11) highlighting characteristic ICT properties. It is apparent that the retransmission stage significantly affects the packet loss as well as the media access delay. The strong relation is introduced by successively resolving the broadcast distribution of data packets. As data is delivered and acknowledged by an increasing number of nodes, the wireless medium is decreasingly contested. This effect is especially strong for the data acknowledgements send by leaf nodes, where a retransmission can experience an up to 19% reduction in packet loss probability. Transmissions exceeding two retransmission experience a virtually free medium and thus experience low packet loss and delay.

TABLE 2 Exemplary simulation results

	Packet Loss Rate [%]			Median MAC Delay [ms]		
RTX Stage	$s=0$	$s=1$	$s=2$	$s=0$	$s=1$	$s=2$
Backbone Node 31						
D-ACK	0.00	0.00	0.00	0.08	0.00	0.00
BD	2.87	0.80	0.00	1.98	1.07	0.05
BD-ACK	2.29	0.73	0.08	2.81	1.22	0.01
S	0.87	0.45	0.00	1.54	1.20	0.05
S-ACK	1.49	0.68	0.85	4.15	1.91	0.00
NR	0.00	0.00	0.00	1.03	0.00	0.00
Leaf Node 11						
D	0.00	0.00	0.00	0.05	0.00	0.00
BD-ACK	31.14	12.26	1.78	6.06	2.45	0.05

5.3 | Model fitness evaluation

The key metric describing the performance of the ICT and the dissemination protocol is the Age of Information (AoI). AoI (first introduced in [38]) captures the freshness of information by combining the update interval at which updates are sent and the time to distribute them. In the context of this publication, it is assumed that optimal performance is achieved by running the control algorithm on data as fresh as possible. Consequentially, the fitness of the stochastic communication model can be verified by comparing the achieved AoI in simulation and emulation. Fitness evaluations focus solely on node- and time-averaged AoI to allow for equivalence comparisons. However, it has to be noted that the performance of the control algorithm may also be effected by peak AoI or individual, node-specific values.

The average AoI $\Delta_i(t)$ at node i at time t is defined as

$$\Delta_i(t) = \frac{1}{N}\sum_{j=1}^{N} \delta_i(t,j), \tag{44}$$

where $\delta_i(t,j)$ is the continuous aging function of information of node j in the buffer of node i. Considering a linear relation between age and elapsing time the continuous aging function is defined as

$$\delta_i(t,j) = t - tx_j[k_i^j], \quad k_i^j < |tx_j|, \tag{45}$$

where tx_j is a vector of transmission times stamps of updates from node j and k_i^j is the index of the most recent received update of information from node j at node i. Finally, the node- and time-averaged AoI is defined as

$$\Delta = \frac{1}{N}\sum_{i=1}^{N} \frac{1}{T-t_0}\int_{t_0}^{T} \Delta_i(t)dt, \tag{46}$$

where $[t_0, T)$ describes the time average period.

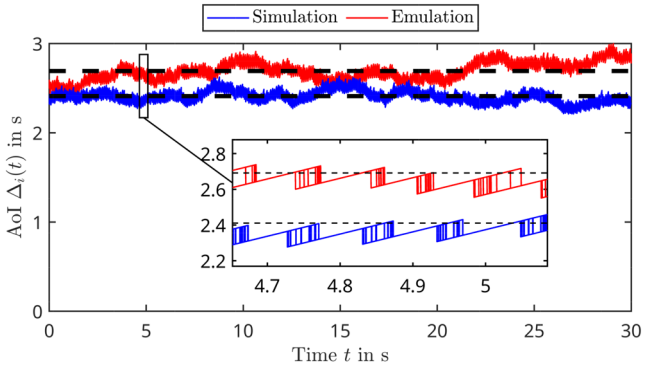

FIGURE 7 Average AoI $\Delta_i(t)$ achieved in simulation and emulation. Node- and time-average AoI Δ plotted as dashed line

The achieved node-specific AoI $\Delta_i(t)$ in simulation and emulation is shown in Figure 7.

Both plots show the characteristic vertical drops in AoI as a node receives new information and can update its local buffer. After the last node receives the update currently being disseminated, AoI in every node is synchronized and ages linearly. This period of stagnation is caused by the signaling overhead of the dissemination protocol to set up the dissemination of the next update. In addition to the node-specific AoIs, the system-wide AoI Δ is given by the dashed line. While the dissemination protocol achieved an average AoI of 2.41s in simulation, it achieved 2.69 s in emulation. The relative difference of 11.7% can be explained by two considerations. First, frame serialization and data manipulation in emulation requires additional processing overhead. Extra delay occurring during the dissemination process causes data to age, and thus AoI to increase. Second, the stochastic model resembles a simplification of the simulated behavior of the communication network. Besides slight numerical inaccuracies, correlation between packet loss events as well as MAC delay observations is lost. However, as these inaccuracies are relatively low and within expectations for switching from simulation to emulation, the model is deemed sufficiently accurate and is deployed for the following evaluations.

6 | EVALUATION IN NORMAL OPERATION

Utilizing the co-emulator described in Section 4, Sections 6 and 7 should demonstrate the performance of the distributed utility maximization under realistic communication network behavior. In doing so, two main objectives are pursued: The first objective is to show the performance of the algorithm with regard to fulfilling the prosumers' needs in a LV grid with a high share of DERs under fluctuating renewable energy supply. Secondly, the robustness of the distributed utility maximization method against communication disturbances should be verified.

To this end, Section 6.1 models an exemplary LV grid in that constitutes the basis for our investigations. Afterwards,

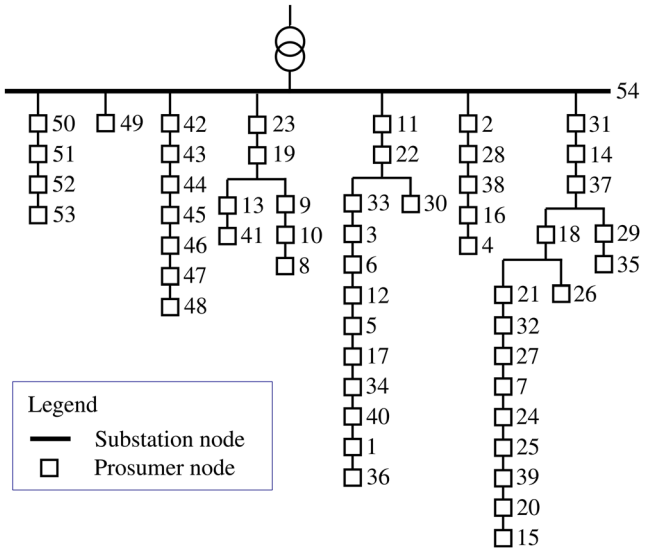

FIGURE 8 Topology of the SimBench *urban-6* test grid with INC numbering.

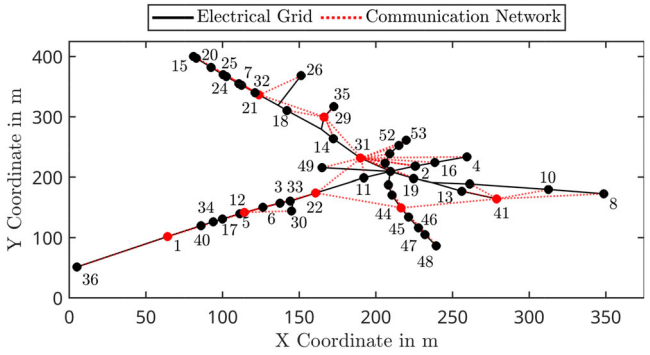

FIGURE 9 Enhanced SimBench model for communication network simulation. Backbone nodes are highlighted in red. Some node labels were omitted for visibility purposes.

simulations are set up and analyzed covering a period of 24 h in Sections 6.2 and 6.3. In these simulations, actual measurements of environmental data from Hamburg are utilized to model the PV plants' maximum power and the prosumers' heat demand. Finally, an investigation of the impact of communication network disturbances is done by means of dedicated simulations of shorter time periods in Section 7.

It should be noted that the ability of the online utility maximization to adhere to keep voltages and currents within their defined limits defined by (14) and (15) has been shown in [17] and is therefore not focussed here. Instead, we emphasize the effects of the newly introduced time-varying priorities, the substation utility functions and of communication network imperfections.

6.1 | LV test grid

The LV test grid utilizes the topology as well as transformer and line impedance data of the *urban-6* LV benchmark grid from the SimBench dataset [39]. The topology and the prosumer specifications are detailed in the following subsections.

6.1.1 | Topology

The *urban-6* grid, which is sketched in Figure 8, is a three-phase LV grid with a radial topology.

The substation transformer has a nominal power of 630kVA. Distribution lines are all cables of type NAYY 4×240SE 0.6/1kV with a current rating of 357A. The documentation [39] provides specifications of the branch lengths and impedance values for the cables and the transformer. Overall, the grid has 7 feeders and a total of 58 LV nodes, 53 of which have connected loads and/or consumers in the SimBench dataset [39].

The SimBench model includes the relative distances between nodes by specifying the length of installed lines. However, this single constraint does not determine absolute node positions which are required for communication network simulations. Additional node placement constraints have to be deployed to derive position coordinates for all INCs. For this, it is assumed that the maximum hop-distance between two nodes affects the performance of the dissemination protocol introduced in Section 5.1 the most. Extending the network by a single hop will require additional backbone nodes and as such additional control overhead for signaling purposes. Consequentially, a worst-case scenario is constructed by respecting the length of installed lines and maximizing a distance metric between all nodes. For this work, the node positioning is based on the squared Euclidean distance between all nodes. The resulting topology is given in Figure 9. The network consists of eight backbone nodes, 46 leaf nodes and requires a minimum communication range of 78m which is inline with the capabilities of the selected IEEE 802.11 ICT. In addition to showing the topological relationship between electrical grid and resulting communication network, the backbone nodes are highlighted in red. The maximum hop-distance of seven hops can be observed between leaf nodes of backbone nodes 1 and 21.

6.1.2 | Prosumer specification

Deviating from the original dataset, each of the 53 nodes contains one prosumer according to the model presented in Section 2. To each prosumer, a residential load profile from the dataset [40] is assigned, specifying the households power consumption on each of the three phases in a one-second resolution. In addition, each prosumer owns a PV plant, a BEV with a charging device and a HP. Therefore, the grid has a high share of DERs: in total 159 DERs that participate in the utility maximization.

A brief overview of how the DER model parameters (refer to Section 2.2 for DER model descriptions) are set is provided below. In addition, Table 6 in the annex contains the parameter values for all 159 DERs.

Battery electric vehicles: A battery size between 35 and 85kWh is randomly assigned to each BEV. Then, the charger power rating is assigned depending on the battery size: single-phase 3.7 kW chargers for batteries up to 50 kWh (14 BEVs in total), three-phase chargers with 11 kW (25 BEVs) and 22 kW (14 BEVs) for larger batteries up to and above 70 kWh, respectively. It is assumed that all chargers feature bidirectional charging, and the charging and discharging efficiency is set to 90%, while the power factor is $\cos\phi = 0.9$.

Photovoltaic power plants: The PV peak power p_{peak} of each prosumer is randomly chosen between 5 and 20kW, and the PV inverter rating equals the peak power, that is, $s_{\text{n}} = p_{\text{peak}}$. Thus, reactive power provision is only possible when the actual active power output is below the peak power. The orientation and inclination angles of the PV modules are determined as follows: Of the 53 PV plants, 34 are assumed to be facing south, with a random deviation between $-45°$ and $+45°$ from a perfect 180°-orientation angle (0° indicates north). The other 19 PV plants have an east-west-orientation, with half of the modules facing east and west, respectively. Again, a random deviation within $-45°$ and $+45°$ from the exact east-west-orientation is applied. Finally, a random module inclination angle between 20 and 60°, measured from the horizontal plane, is assigned to each PV plant.

Heat pumps: To specify the heat pumps, the heat source (air, brine or groundwater) and heat sink (floor heating or radiator heating) are randomly set for each HP. They define the COP curves as mentioned in Section 2.2.3. Then, an annual heat demand Q_{annual} is determined by choosing a value between 20, 000 and 80,000 kWh. Based on the annual heat demand, the electrical minimum and maximum pump power values $p_{\text{min,on}}$ and p_{max} are chosen based on publicly available data from commercial modulating HPs. The power factor is set to $\cos\phi = 0.85$. The heat storage size is randomly selected within 1000 and 2000L. Heat losses are calculated assuming a temperature of $\vartheta_{\text{amb}} = 20°\text{C}$ around the storage. The admissible temperature ranges applying to the heat storage are [35°C, 45°C] for floor heating and [40°C,60°C] for radiator heating, respectively.

6.2 | Simulation setting

With the test grid described above, simulations of 24-h-periods should demonstrate our algorithm's ability to satisfy prosumer needs in spite of fluctuating renewable energy supply. The setup of all time-dependent quantities and the optimization algorithm parameters are described in this section.

The general approach is as follows: we fix the 24 h simulation period as well as various environmental and user data. Then, we vary the substation target power curve and the substation power limits to reflect different availability of power supply in the superordinate grid (e.g. due to different wind conditions). The utility maximization should autonomously adapt to the different conditions and utilize the flexibility of the DERs such that prosumers are satisfied, without any manual input.

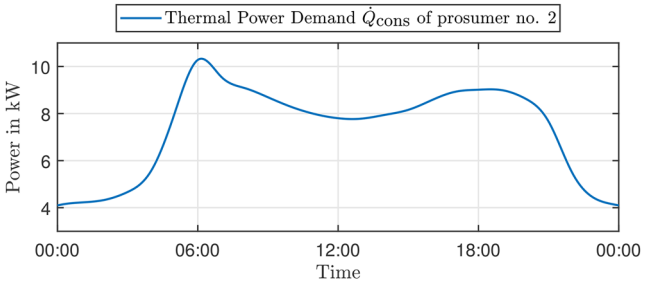

FIGURE 10 Heat demand of prosumer no. 2 during the simulation period

6.2.1 | Environmental data and prosumer behavior

On the basis of environmental data measurements from the Hamburg Weather Mast [41], we choose a day with average overall solar irradiation as the simulation period, namely the 9th April 2021. The trends of direct and diffuse irradiation are input to the PV plant models to determine the maximum output power. Besides solar irradiation, the corresponding air temperature trend is utilized to specify the air–water heat pumps' COP. Groundwater temperature ϑ_{water} and brine temperature ϑ_{brine} are assumed constant throughout the day, with $\vartheta_{\text{water}} = 5°\text{C}$ and $\vartheta_{\text{brine}} = -2.7°\text{C}$. Both curves have a 1-min resolution, so the data is interpolated in between samples to support the simulation stepsize, which is 0.2 s. Figure 10 shows an exemplary prosumer heat demand curve. Note that due to the SLP based approach detailed in Section 2.2.3, the other prosumer's heat demand curves are similar.

With regard to the prosumer behavior, BEV charging times and battery states need to be modelled. We assume that at the beginning of the day, all BEVs are at their charging station, and randomly assign SoC values between 50% and 90%. In the morning, half of the BEVs depart at random times between 7:00 and 9:00. On the contrary, every second BEV remains at its charging station throughout the whole day. The BEVs return between 15:30 and 17:30 with SoCs between 20% and 50%. Of these BEVs, 13 depart for a second journey later that evening. Upon arrival, the BEV owners enter their next departure time at the charging station. Furthermore, they define a target SoC of 80%. These data are required to calculate the dynamic priorities as detailed in Section 3.3.2. To keep a minimum charge for spontaneous trips, a lower SoC limit of 25% is set for each BEV, that is, discharging is prohibited below this limit.

6.2.2 | Substation settings

The substation utility functions for active and reactive power specified in Section 3.3.3 each contain three constant parameters: the maximum substation utility $\Phi_{s,0}^{p/q}$, the weighting factor $w_s^{p/q}$ and the marginal utility magnitude limit $\gamma_{\text{max}}^{p/q}$. Note that

TABLE 3 Stepsize parameters for the online optimization algorithm

Parameter	Symbol	Value
Primal stepsize	α	50W^{-1}
Dual stepsize (voltage)	α_v	25V^{-1}
Dual stepsize (currents)	α_i	0.4A^{-1}
Dual stepsize (power)	α_s	1.89W^{-1}

$\Phi_{s,0}$ does not affect the solution of the utility maximization problem (21), but only the objective function value at the solution. Therefore, it is set to zero. The active power weighting factor is chosen as $w_s^p = 2 \cdot 10^{-5}$, such that the marginal substation utility is $\Phi_s' = -1$ and $\Phi_s' = 1$ when the substation power deviates from the target value $\Phi_{s,t}$ by 50 kW and -50 kW, respectively. The reactive power weight is $w_s^q = 4 \cdot 10^{-5}$, and maximum marginal utilities $\gamma_{\max}^p = 4$ and $\gamma_{\max}^q = 2$ are applied.

Apart from the constant parameters, target values $p_{s,t}$ and $q_{s,t}$ as well as limits $\underline{p}_s$, $\overline{p}_s$, $\underline{q}_s$ and $\overline{q}_s$ are to be specified for the substation active and reactive power. These parameters are not constant, but vary with time. As stated above, we specify two variants for the active power and denote these by *Scenario 1* and *Scenario 2*. Scenario 1 corresponds to an increased power availability from the MV grid in the first half of the day. Until 11 o'clock, the target active power is $p_{s,t} = 100$ kW, and the limits are $\underline{p}_s = 0$ kW and $\overline{p}_s = 200$ kW, respectively. Between 11:00 and 13:00, all three parameters linearly change to $p_{s,t} = 0$ kW, $\underline{p}_s = -50$ kW and $\overline{p}_s = 50$ kW. Thus, a self-sufficient LV grid operation is favored in the second half of the day, and rather tight limits are set for power consumption from or injection into the MV grid.

In Scenario 2, the target and limit power curves are mirrored at noon: now, self-sufficiency is provoked in the first half of the day, and power availability from the MV grid assumed in the second half of the day.

In regard to the reactive substation power, the MV grid favors a balanced LV grid in both scenarios. Therefore, the reactive power target value is $q_{s,t} = 0$VAr. The reactive power limits are $\underline{q}_s = -50$ kVAr and $\overline{q}_s = 50$ kVAr.

6.2.3 | Algorithm parameters

The primal and dual stepsize parameters of the online optimization algorithm are set according to Table 3. They were determined by parameter tuning and refer to a cycle time of $T_s = 1s$. Their units are chosen such that the utility is dimension-free.

Furthermore, an admissible voltage band of $+/-5\%$ around the nominal voltage is defined, that is, $\underline{v} = 380$V and $\overline{v} = 420$V. The branch current limits are set according to the cables' thermal limit current.

Finally, the characteristic points of the priority functions defined in Section 3.3.2 are noted in Tables 4 and 5 for BEVs and HPs, respectively.

TABLE 4 Sample points of BEV priority functions

Time Margins			Priority		
$T_{b,\min}$	$T_{b,n}$	$T_{b,\max}$	$w_{\max}$	w_n	$w_{\min}$
0.1h	1h	5h	2	1	0.5

TABLE 5 Sample points of HP priority functions

	Temperature			Priority		
	$\vartheta_{\min}$	ϑ_n	$\vartheta_{\max}$	$w_{\max}$	w_n	$w_{\min}$
Floor heating	35°C	40°C	45°C	2	1	0.125
Radiator heating	40°C	50°C	60°C	2	1	0.125

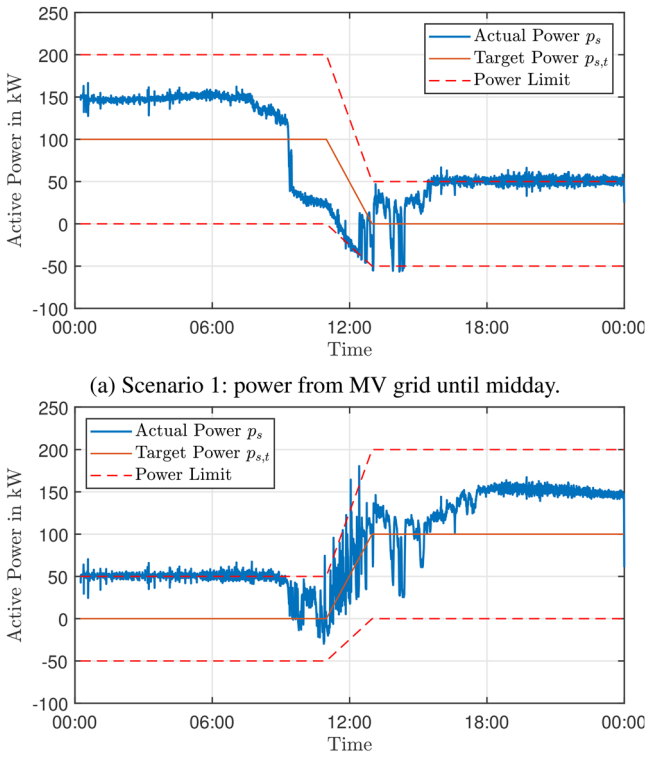

(a) Scenario 1: power from MV grid until midday.

(b) Scenario 2: power from MV grid from midday on.

FIGURE 11 Transformer power limits and actual active power p_s in both scenarios. Positive values signify power flow into the LV grid

6.3 | Simulation results

Now, we analyze and compare the simulation results of the 24-h-simulations for Scenario 1 and Scenario 2. To this end, the figures in this section generally contain two diagrams, one for Scenario 1 and one for Scenario 2, showing the same quantities.

The substation transformer active power is shown in Figure 11. In both scenarios, p_s is mostly positive and exceeds the target value $p_{s,t}$. This implies that the prosumers in the LV grid mostly prefer to draw active power from the MV grid, and to an extent greater than preferred by the MV grid. In times of

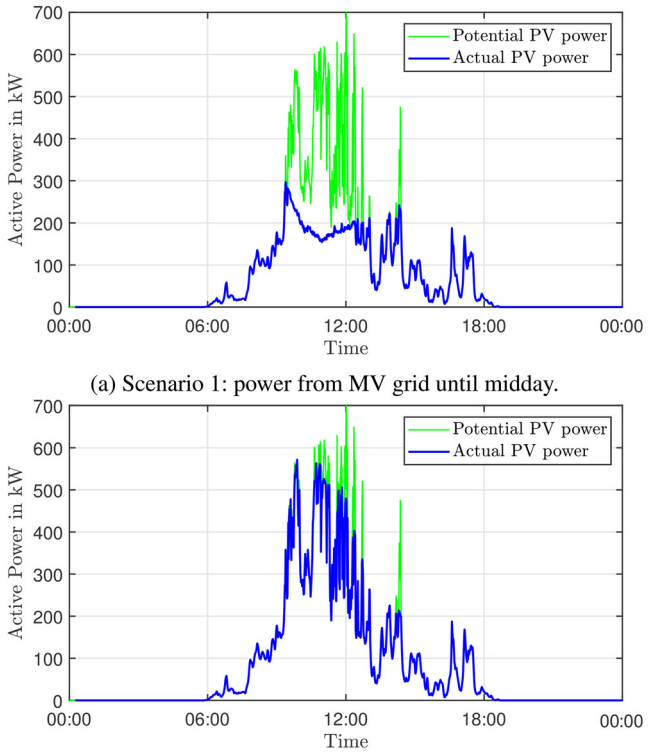

(a) Scenario 1: power from MV grid until midday.

(b) Scenario 2: power from MV grid from midday on.

FIGURE 12 Actual an potential aggregated power output of the 53 PV plants in the LV grid

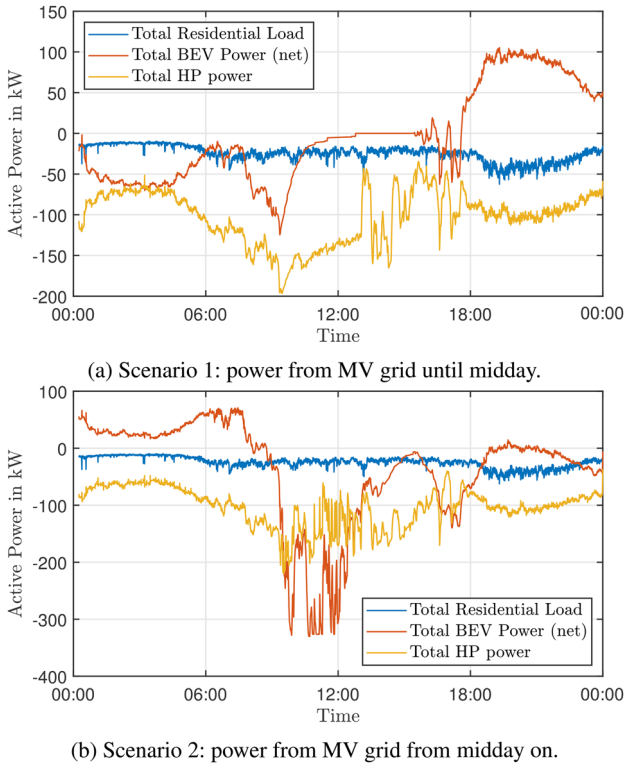

(a) Scenario 1: power from MV grid until midday.

(b) Scenario 2: power from MV grid from midday on.

FIGURE 13 Aggregated power of residential loads, BEVs and HPs. Positive values denote power injection into the LV grid

higher power availability from the MV grid, that is, in Scenario 1 until midday and in Scenario 2 from midday on, the power limit is not reached. This indicates that the marginal utilities of DERs and the substation are balanced, for example, for a consumer in the LV grid, the utility gain from increasing its power consumption would equal the resulting substation utility loss. During the other half of the day, when the power limits are tighter and the target value is $p_{s,t} = 0$, the upper limit of $\overline{p}_s = 50$ kW is reached. Apparently the INCs perform well in preventing limit violations. Note that small deflections are inevitable for the dual approach when disturbances like fluctuating residential load are present.

In both scenarios, though more severe in Scenario 1, p_s drops at 9:20. This is explainable by a sudden rise of PV power in the LV grid, which is depicted in Figure 12. The difference between the green and the blue lines in Figure 12 is the curtailed PV power. A curtailment of PV power indicates that the energy storage systems in the LV grid are full and a (further) power transfer to the MV grid is undesired. In both scenarios, this is the case around midday, but PV power curtailment happens earlier and—in total—to a significantly higher extent in Scenario 1. This is reasonable, as the power consumption from the MV grid in Scenario 1 is higher throughout the morning. Therefore, energy storage systems (i.e. the BEV batteries and the HP thermal storage) can be charged in the morning and sooner reach their capacity limit when the PV plants ramp up their power output. In Scenario 2, on the other hand, the storage levels are lower, so a higher share of the solar power around midday can be utilized to charge the energy storage.

The trends of aggregated PV and BEV power in Figure 13 support this analysis. In Scenario 1, the net aggregated BEV power (i.e. injection minus consumption) is negative in the morning, so on average, the batteries are charged. In Scenario 2, the situation is very different: until 9 o'clock, the BEVs feed power into the grid, compensating for the limited power availability from the MV grid. Afterwards, it is noticeable that the BEVs are charged according to the PV supply, whereas in Scenario 1, charging power drops to zero at noon, indicating full batteries. In the evening, the situation is reversed: now, BEVs feed back power into the grid in Scenario 1. This aggregated view shows how the flexibility provided by BEVs is utilized by the optimization to cope with different power availability scenarios.

The aggregated view, however, does not reveal that individual BEV charging curves can differ a lot, depending on the scheduled departures. Therefore, exemplary trends are depicted in Figure 14 for the BEV no. 21, which stays at the charging station the whole day, and BEV no. 49, which leaves in the morning and again in the evening. Both BEVs are equipped with an 11kW charger. In both scenarios, BEV 49 is sufficiently charged to reach its SoC target of 80% until the first departure at 8:17. Note that this holds true for all BEVs that depart in the morning. During the second stay at the charger, from 18:37 till 19:40, BEV 49 is charged with high power, but the short duration of the stay limits the reachable SoC.

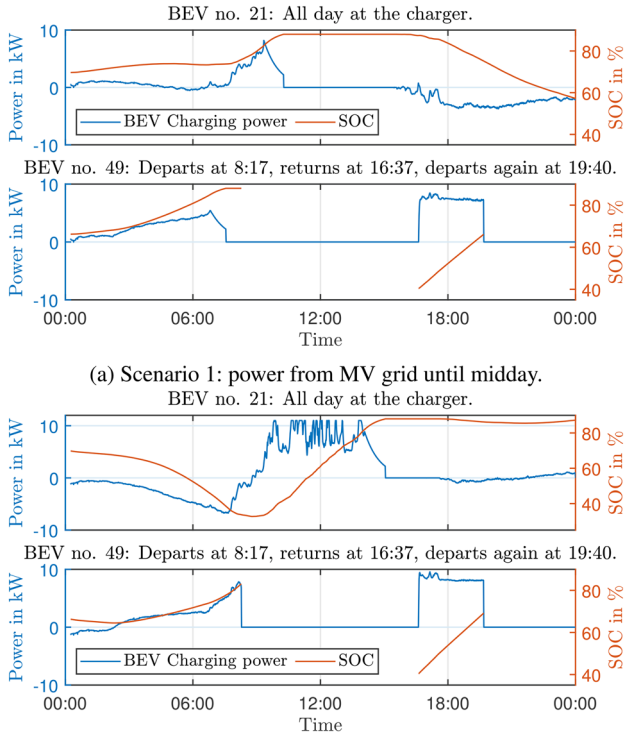

(a) Scenario 1: power from MV grid until midday.

(b) Scenario 2: power from MV grid from midday on.

FIGURE 14 Charging Power and SoC comparison for two BEVs, one that remains at the charger (top), and one that departs twice (bottom)

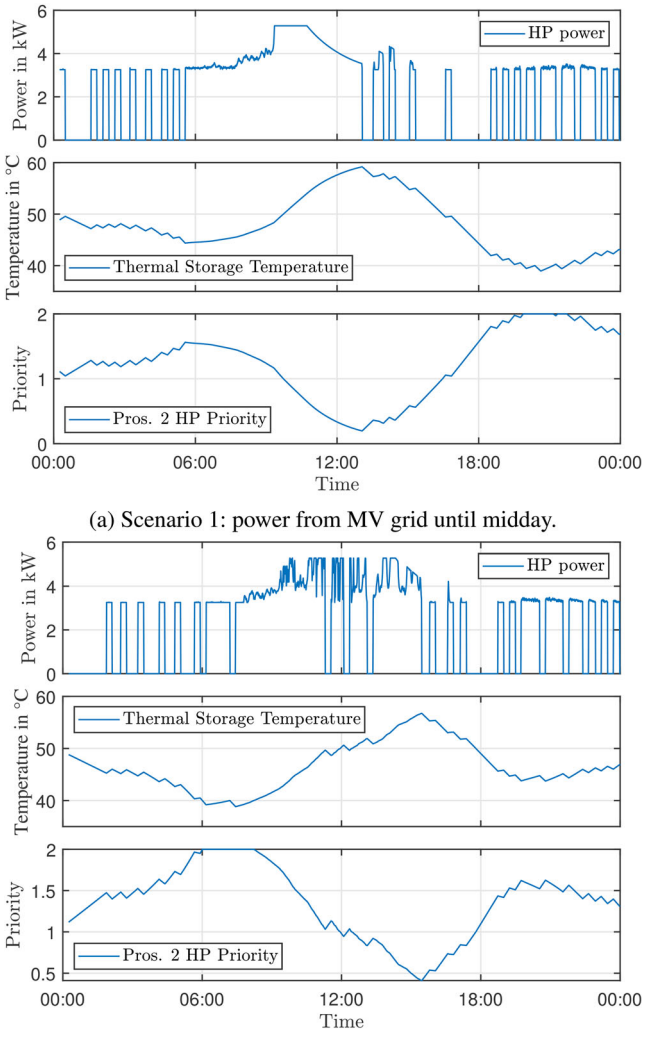

(a) Scenario 1: power from MV grid until midday.

(b) Scenario 2: power from MV grid from midday on.

FIGURE 15 Electrical power consumption, thermal storage temperature and priority of HP no. 2

In contrast to BEV 49, the trends for BEV 21 differ significantly in the two scenarios. While BEV 21 is slightly charged in the first eight hours of the day in Scenario 1, it is significantly discharged in the same period in Scenario 2. The opposite behavior occurs in the evening, when BEV 21 is discharged in Scenario 1. In both cases, the battery is fully charged during PV power availability around midday. As reflected in the aggregated view in Figure 13, a lot more energy from PV plants is required in this charging period in Scenario 2. In conclusion, the individual BEV charging trends indicate that the dynamic prioritization (see 3.3.2) for BEVs indeed leads to a flexibility usage that respects the prosumers' needs.

Having analyzed the transformer power, PV plants and BEVs, we now focus on the HPs. The aggregated HP power trend in Figure 13 is similar in both scenarios: Moderate power consumption in the morning, high power consumption around midday and a smaller peak in the evening, and it can be noted that the peak of the electric power consumption does not coincide with the peak of the heat demand shown in Figure 10. Thus, it appears that the HPs power consumption is also aligned with the PV power supply to a certain extent. However, compared to BEVs, differing substation power preferences apparently have a minor impact on the flexibility provided by the HPs in the simulated use case. The exemplary trends of a HP's electrical power consumption, thermal storage temperature and priority depicted in Figure 15 still reveal certain differences between Scenarios 1 and 2. In both cases, the thermal storage is discharged in the morning hours, but to a larger extent in Scenario 2, when power consumption from the MV grid is strictly limited. Here, the temperature reaches its lower limit of 40°C at 6:00, corresponding to a maximum priority of 2 (see Table 5). Note that further discharge is then prohibited by the pump itself, that is, it enforces to switch the pump on. Similar to the BEVs, the thermal storage is then charged during solar power availability in both scenarios. In the afternoon, it is discharged again. Now, the discharge is more significant in Scenario 1, where the lower temperature limit is reached at 20:00. This leads to the conclusion that HPs are also affected by the varying transformer preferences.

In addition, the power trends in Figure 15 clearly show the switching behavior of the modulating HPs. While it seems that the optimization performance is not significantly impaired by this switching behavior, a detailed analysis is out of the scope of this work.

Overall, the simulations demonstrate that the distributed real-time utility maximization implemented in the INCs performs well in fulfilling the prosumers' needs under different MV power

availability scenarios. In doing so, it utilizes the available DERs' flexibility with a high degree of autonomy, that is, little manual user input. It should be noted that the simulations cover a certain use case with particular environmental data and specific DER models. Therefore, the results cannot be generalized. Nonetheless, we are positive that the approach will cope well in other use cases. This is mostly due to the feedback-based algorithm that constantly adapts to changing conditions. It also enables a rather generic and simple interface between INC and DERs, requiring little model information and frequent updates of only actual power values and the relevant DER states for priority calculation. An inherent limitation stems from the fact that the feedback-based approach does not incorporate any predictions, for example, weather forecasts. This hinders the integration of dispatch decisions for DERs that require, for example, ramp-up times and minimum switch-on durations. It is a common limitation of online optimization approaches, and combining forecasts and online optimization could be an interesting future research direction.

For the sake of completeness, it should be noted that neither voltage nor current limits are violated in the simulations. This is not surprising due to the rather tight substation power limits of at most 200 kW compared to the rated transformer power of 630 kVA. Furthermore, the substation reactive power target $q_{s,t} = 0$ is met in both scenarios with little fluctuations. This indicates that the PV plants, which are the only DERs that allow to adjust their reactive power, perform well in compensating the reactive power of inflexible loads and other DERs.

7 | EVALUATION UNDER COMMUNICATION NETWORK DEGRADATION

As with all networked control systems the proposed control method requires the timely exchange of information between INCs. Nominal operation assumes that every INC takes part in the optimization process and measurement errors are consistent as well as bounded. However, as wireless communication systems can only be hardened against failures to a limited degree, full or partial loss of connectivity remains possible. Therefore, two additional evaluations are conducted and discussed in this section. First, the relation between AoI and control performance is investigated by analyzing the difference in substation transformer power p_s in multiple scenarios with decreasing communication network performance. Afterwards, the resilience of the control method as well as the communication network against INC failure is evaluated.

7.1 | Simulation setting

The simulations conducted in this section share most of the simulation settings used for scenario 2 defined in the previous Section 6. However, as both evaluation focus on the impact of the communication network, no full-day simulations are required.

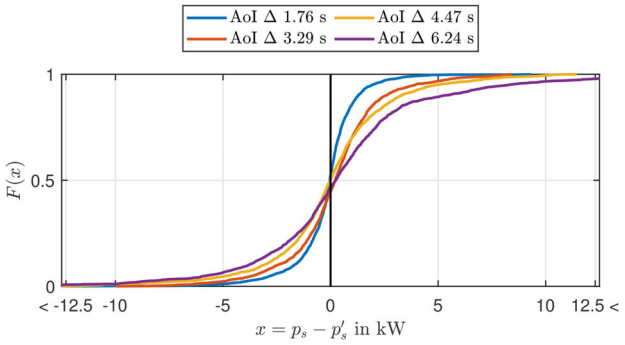

FIGURE 16 Distribution functions for the difference in power flow at the substation transformer for scenarios with increasing AoI

To analyze the effects of increased data aging, a 45 min period with large variation in PV generation is selected. Increased information age in these highly dynamic scenarios impacts the measurement accuracies the most. The evaluation is conducted on the 45 min period starting from 11:00 and includes a 5 min warm-up time.

A benchmark run is conducted in which all delays which may occur in the communication network are set to zero. The so achieved ground-truth constitutes the best possible response of the proposed control method as each INC has perfect knowledge about all measurement information of other INCs. The aggregated effect of each INC's responses are well-captured in the power flow over the substation transformer. We denote the substation power in the benchmark run as p'_s. Any deviation from this response is assumed to be an unwanted artifact introduced by the delayed reception of measurements. The distribution of the difference $p_s - p'_s$ between substation transformer power flow p_s and the ground-truth is selected as the key performance indicator.

For analyzing the impact of full INC failures, a time period with high BEV demand but limited supply from local PV and superordinate MV grid is selected. During these periods, the main objective of the control method is to coordinate the BEVs charging processes without exceeding the maximum substation power $\overline{p}_s$. The period of the day during which this situation is the most pronounced is in the early morning hours, where the thermal storage of HPs are depleted by the night, no PV generation is available and most of the BEVs are charging to meet their departure deadline. For this evaluation, a 45 min period starting from 2:00 AM was selected. After a brief warm-up period of 22 min, INCs start to fail and drop out of the communication network every 30 s until 37 INCs are disconnected. To maintain rudimentary service quality in the event of full communication network failure, INCs fallback to a simple local control strategy.

7.2 | Simulation results

First, we look at the simulation results concerning the effects of increasing AoI on the substation power flow. Figure 16 shows the cumulative distribution functions for the difference $p_s - p'_s$.

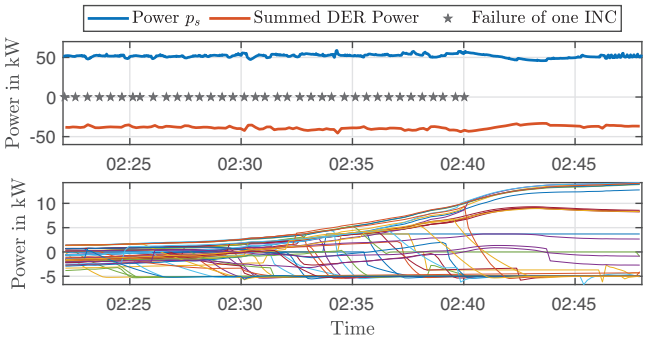

FIGURE 17 Actual power plots for substation power and aggregated INC powers as well as INC specific plot for scenario with node failures

A perfect match between results would be indicated by a vertical line, as every power flow sample would be same and the set of difference would consist only of zeros. On the other hand, if the observed response does not share any resemblance with the optimal one, the distribution would appear as a flat, horizontal line, if one considers the plot limits. The evaluation spanning 45 min were conducted for four configurations each achieving an AoI of 1.76 s, 3.29 s, 4.47 s and 6.24 s, respectively. The observed density functions for all evaluations follow the shape of normal distributions with zero mean. With increasing AoI, the variance of the normal distribution increases from $\sigma = 1.54$ kW to $\sigma = 4.4$ kW for the best and worst case.

The results show a significant correlation between the AoI achieved by the communication network and the effect on the selected control variable, the power flow p_s. As measurements and information about DER setpoints are updated less frequently, INCs have to conduct optimization steps with an increasingly stale set of input values. The control cycle time of 1 s does not yield significant benefits, if the underlying information remains almost the same in high AoI scenarios. The observed time lag introduces additional dead-times into the control loop and may lead to unwanted oscillations or dynamics. However, even in the extreme case of an AoI of 6.24 s, the deviations from the optimal response is mostly bounded by ± 10 kW. Considering the limited deviation as well as the observed zero mean, it can be concluded that the proposed algorithm remains stable even in the event of moderate communication network degradation. Furthermore, the AoI performance metric directly correlates with the expected control method's performance and constitutes a useful abstraction for the networked control system. An improvement in AoI improves the performance of the proposed control method.

In addition to the soft degradation of the communication network caused by increased delays, INC connectivity may fail completely. In such an event, failing INCs may fall back to a backup strategy to still maintain a limited service quality for connected DERs. All remaining, actively controlled INCs have to compensate for the actions of failing INCs as they are not actively communicating anymore. Figure 17 shows selected results to display the resilience of the proposed control method in the case of massive connectivity loss. The first plot shown in Figure 17 shows the actual power measured at the substation transformer, the aggregated DER actual powers as well as the timestamps at which INCs lost connection. The substation power limit of 50 kW is maintained consistently even in the case of the successive failure of 37 INCs. In fact, there is no visible indication that INCs may have failed, as the remaining INCs still get periodic power flow measurements from the substation and can adjust their local DER power setpoints accordingly. Most of the substations power budget is consumed by the DERs as general household power consumption is still low at 2:00 in the morning.

A more prominent effect of INC loss of connectivity can be observed in the INC specific nodal powers shown in the second plot of Figure 17. At the beginning of the evaluation, the proposed control method causes the INCs to share the available substation power budget according to their departure deadline priorities. However, as INCs disconnect, the default parametrization of the backup strategy allows the failed INCs to consume up to 5 kW which is higher than the power in equilibrium. The increased power consumption by failed INCs forces other, still connected INCs to decrease their power consumption. As more and more INCs start to fail, their default behavior may even force the remaining INCs to start injecting power by discharging their BEVs. This trend can be observed after around 2:30 and keeps increasing until the target number of INCs failed. As the capacity of the still actively managed BEVs is finite, it is to be expected that after sufficient time, no additional power from INCs can be injected into the grid and consequentially, the substation power has to increase. This also highlights one key property of the proposed control method. INCs try to abide to grid constraints as long as possible, by using the available flexibility of DERs until all resources are depleted.

In this section, we showed how degraded performance of the communication network effects the performance and behavior of the proposed control method. In the case of soft degradation caused by additional delay and subsequent higher AoI, the proposed method is able to maintain close to optimal performance, although with higher variation in grid metrics such as the substation power flow. Additionally, even in the case of multiple full connectivity losses, the proposed control method upholds the grid constraints as long as resources allow it. Since only a limited number of metrics could be examined within the scope of this paper, a fully qualitative statement on the resilience of the proposed control method is not possible. However, the result shown in this evaluation indicate a favorable behavior of the control method, even in the case of significant communication network degradation.

8 | CONCLUSION AND OUTLOOK

This paper proposes a distributed real-time control method for DERs in LV grids, aiming at an optimal utilization of the fluctuating renewable energy supply and the flexibility provided by DERs in order to fulfill the prosumers' needs. To this end, time-varying utility functions for DERs and the power flow across the substation quantify the prosumers' needs. The

resulting utility maximization problem is then solved by a distributed online primal-dual gradient algorithm that relies on a frequent measurement broadcast among the INCs. A real-time flooding protocol is introduced to handle the communication load. To evaluate the performance of the proposed control method and the impact of the communication network, a co-emulation platform is set up consisting of a RTDS for LV grid simulation and a communication network emulator.

The evaluation of an exemplary use-case demonstrates that the proposed utility-maximizing control effectively utilizes the energy storage capacity of BEVs and HPs to meet the prosumers' needs in different power availability scenarios. When necessary, it curtails the power generation from PV plants. Furthermore, it exhibits a certain robustness when the communication delay is moderately increased; that is, the control remains stable. Finally, individual INC connectivity loss is well compensated for by the remaining INCs.

In our future work, we intend to integrate the co-emulator in a Power-Hardware-in-the-Loop environment to investigate the control method's applicability using actual controller and power hardware. Also, an extension of the control method towards a hierarchically distributed MV and LV grid control is envisaged. Moreover, a possible research direction targets the tighter coupling between control and communication network; for instance, controller parameters could adapt to changing communication network properties. Finally, future research regarding the communication network could focus on eliminating the need for backbone nodes and embracing a fully distributed communication network.

NOMENCLATURE

For reference, the list below explains the notation used in this paper as well as the most relevant symbols and sets. However, mathematical quantities are specified in detail upon occurrence throughout the manuscript.

Notation:

x, y, z	scalars
$\boldsymbol{x}, \boldsymbol{y}, \boldsymbol{z}$	vectors
X, Y, Z	matrices or scalars
$\lvert\cdot\rvert$	magnitude for scalars, number of elements for sets
$[\cdot]_{\geq 0}$	projection onto the nonnegative orthant
$[\cdot]_{[x,y]}$	projection onto the interval $[x, y]$
$\underline{x}, \overline{x}$	lower and upper limit of x

Symbols for variables and functions:

v	electric voltage
i	electric current
p	active power
q	reactive power
s	apparent power
Φ	utility
t	time
w	priority factor
S	sensitivity matrix
α	stepsize parameter
λ, μ, ν, ξ	dual multipliers

Sets:

$\mathcal{N}$	set of nodes in the electric grid
$\mathcal{B}$	set of branches in the electric grid
$\mathcal{P}$	set of prosumers in the electric grid
$\mathcal{N}_{\mathcal{P}}$	set of prosumer nodes
$\mathcal{C}$	set of DERs
$\mathcal{C}_r$	set of DERs of prosumer r
$\mathbb{R}$	set of real numbers
$\mathbb{C}$	set of complex numbers

AUTHOR CONTRIBUTIONS

Hanko Ipach: Conceptualization, investigation, methodology, software, validation, visualization, writing - original draft, writing - review and editing. Leonard Fisser: Conceptualization, investigation, methodology, software, validation, visualization, writing - original draft, writing - review and editing. Christian Becker: Conceptualization, funding acquisition, methodology, project administration, resources, supervision, writing - review and editing. Andreas Timm-Giel: Conceptualization, funding acquisition, methodology, project administration, resources, supervision, writing - review and editing.

ACKNOWLEDGEMENTS

This work was funded by the German Research Foundation (Deutsche Forschungsgemeinschaft, DFG) as part of the *OUREL* project with reference number 426655646.

CONFLICT OF INTEREST

The authors declare no conflict of interest.

DATA AVAILABILITY STATEMENT

The data that support the findings of this study are available from the corresponding author upon reasonable request.

ORCID

Hanko Ipach https://orcid.org/0000-0003-1433-6157
Leonard Fisser https://orcid.org/0000-0003-1856-3787
Christian Becker https://orcid.org/0000-0002-5707-345X
Andreas Timm-Giel https://orcid.org/0000-0002-5998-6113

REFERENCES

1. Aziz, T., Ketjoy, N.: Pv penetration limits in low voltage networks and voltage variations. IEEE Access 5, 16784–16792 (2017)
2. Chen, X., Dall'Anese, E., Zhao, C., et al.: Aggregate power flexibility in unbalanced distribution systems. IEEE Trans. Smart Grid 11(1), 258–269 (2020)
3. Guggilam, S.S., Dall'Anese, E., Chen, Y.C., et al.: Scalable optimization methods for distribution networks with high pv integration. IEEE Trans. Smart Grid 7(4), 2061–2070 (2016)
4. Cain, M.B., O'Neill, R.P., Castillo, A.: History of optimal power flow and formulations, Tech. Rep. (2012)
5. Bernstein, A., Dall'Anese, E.: Real-time feedback-based optimization of distribution grids: A unified approach. IEEE Trans. Control Netw. Syst. 6(3), 1197–1209 (2019)
6. Gan, L., Low, S.H.: An online gradient algorithm for optimal power flow on radial networks. IEEE J. Sel. Areas Commun. 34(3), 625–638 (2016)

7. Picallo, M., Bolognani, S., Dörfler, F.: Closing the loop: Dynamic state estimation and feedback optimization of power grids. Electr. Power Syst. Res. 189, 106753 (2020). https://www.sciencedirect.com/science/article/pii/S0378779620305563
8. Hauswirth, A., Zanardi, A., Bolognani, S., et al.: Online optimization in closed loop on the power flow manifold. In: 2017 IEEE Manchester PowerTech, pp. 1–6. IEEE, Piscataway (2017)
9. Tang, Y., Dvijotham, K., Low, S.: Real-time optimal power flow. IEEE Trans. Smart Grid 8(6), 2963–2973 (2017)
10. Ospina, A.M., Bastianello, N., Dall'Anese, E.: Feedback-based optimization with sub-weibull gradient errors and intermittent updates. IEEE Control Syst. Lett. 6, 2521–2526 (2022)
11. Bernstein, A., Dall'Anese, E., Simonetto, A.: Online primal-dual methods with measurement feedback for time-varying convex optimization. IEEE Trans. Signal Process. 67(8), 1978–1991 (2019)
12. Picallo, M., Liao McPherson, D., Bolognani, S., et al.: Cross-layer design for real-time grid operation: Estimation, optimization and power flow. Electr. Power Syst. Res. 212, 108378 (2022). https://www.sciencedirect.com/science/article/pii/S0378779622005417
13. Guo, Y., Zhou, X., Zhao, C., et al.: Solving optimal power flow for distribution networks with state estimation feedback. In: 2020 American Control Conference (ACC), pp. 3148–3155. IEEE, Piscataway (2020)
14. Picallo, M., Ortmann, L., Bolognani, S., et al.: Adaptive real-time grid operation via online feedback optimization with sensitivity estimation. Electr. Power Syst. Res. 212, 108405 (2022). https://www.sciencedirect.com/science/article/pii/S0378779622005582
15. Ortmann, L., Prostejovsky, A., Heussen, K., et al.: Fully distributed peer-to-peer optimal voltage control with minimal model requirements. Electr. Power Syst. Res. 189, 106717 (2020)
16. Ortmann, L., Hauswirth, A., Caduff, I., et al.: Experimental validation of feedback optimization in power distribution grids. Electr. Power Syst. Res. 189(2), 106782 (2020). http://arxiv.org/pdf/1910.03384v2
17. Ipach, H., Fisser, L., Becker, C., et al.: Utility-based operation management for low voltage distribution grids using online optimization. e&i Elektrotechnik und Informationstechnik 138(8), 495–504 (2021)
18. Eger, K., Killat, U.: Resource pricing in peer-to-peer networks. IEEE Commun. Lett. 11(1), 82–84 (2007)
19. Li, M., Tran, P.N., Tütüncüoğlu, H.K., et al.: Coordinated radio resource allocation in lte femtocell cluster considering transport limitations. In: 2015 IEEE International Conference on Communications (ICC), pp. 3113–3118. IEEE, Piscataway (2015)
20. Heuck, K., Dettmann, K.D., Schulz, D.: Elektrische Energieversorgung: Erzeugung, Übertragung und Verteilung elektrischer Energie für Studium und Praxis. 9th ed., Springer Vieweg, Lehrbuch, Wiesbaden (2013)
21. Kron, G.: Tensor Analysis of Networks. John Wiley & Sons, New York (1939)
22. Abur, A., Gómez Expósito, A., Gómez Expósito, A.: Power system state estimation: Theory and implementation. Power Engineering, vol. 24. CRC Press and Dekker, Boca Raton, Florida and New York and Basel (2004). http://www.loc.gov/catdir/enhancements/fy0647/2004300427-d.html
23. Klucher, T.: Evaluation of models to predict insolation on tilted surfaces. Solar Energy 23(2), 111–114 (1979)
24. Quaschning, V.: Regenerative Energiesysteme: Technologie - Berechnung - Simulation; 119 Tab. 9th ed. Hanser eLibrary, München: Hanser, (2015). http://ebooks.ciando.com/book/?bok_id=1914994
25. Röhrenbeck, S.E.A.: Wärmepumpen und Speichersysteme als Flexibilitäten im Kontext des Zellularen Ansatzes [Dissertation]. Technische Universität Kaiserslautern, Kaiserslautern, (2019)
26. Ruhnau, O., Hirth, L., Praktiknjo, A.: Time series of heat demand and heat pump efficiency for energy system modeling. Sci. Data 6(1), 189 (2019)
27. Ipach, H., Stock, S., Becker, C.: A modified branch-current based algorithm for fast low voltage distribution grid state estimation using smart meter data. ETG Congress 2021, pp. 1–6. (2021)
28. Candas, S., Zhang, K., Hamacher, T.: A comparative study of benders decomposition and admm for decentralized optimal power flow. In: IEEE Power & Energy Society Innovative Smart Grid Technologies Conference (ISGT), vol. 22020, pp. 1–5. IEEE, Piscataway (2020)
29. Tan, S., Song, W.Z., Dong, Q., et al.: SCORE: Smart-Grid common open research emulator. In: 2012 IEEE Third International Conference on Smart Grid Communications (SmartGridComm), pp. 282–287. IEEE, Piscataway (2012)
30. Teng, J.H.: A direct approach for distribution system load flow solutions. IEEE Trans. Power Delivery 18(3), 882–887 (2003)
31. Stolpmann, D., Timm-Giel, A.: FlowEmu: An open-source flow-based network emulator. Electronic Communications of the EASST 80, (2021)
32. Linux Foundation: NetEm (2022). https://wiki.linuxfoundation.org/networking/netem. Accessed 03 June 2022
33. Gungor, V.C., Sahin, D., Kocak, T., et al.: A survey on smart grid potential applications and communication requirements. IEEE Trans. Ind. Inf. 9(1), 28–42 (2013)
34. Ghorbanian, M., Dolatabadi, S.H., Masjedi, M., et al.: Communication in smart grids: A comprehensive review on the existing and future communication and information infrastructures. IEEE Syst. J. 13(4), 4001–4014 (2019)
35. Fisser, L., Timm-Giel, A.: Minimizing age of information for distributed control in smart grids. In: 2021 IEEE International Conference on Communications, Control, and Computing Technologies for Smart Grids (SmartGridComm), pp. 1–7. IEEE, Piscataway (2021)
36. Farazi, S., Klein, A.G., McNeill, J.A., et al.: On the age of information in multi-source multi-hop wireless status update networks. In: 2018 IEEE 19th International Workshop on Signal Processing Advances in Wireless Communications (SPAWC), pp. 1–5. IEEE, Piscataway (2018)
37. Lünsdorf, O., Scherfke, S.: Simpy - discrete event simulation for python. (2022). https://simpy.readthedocs.io/en/latest/. Accessed 03 June 2022
38. Kaul, S., Gruteser, M., Rai, V., et al.: Minimizing age of information in vehicular networks. 2011 8th Annu. IEEE Communications Society Conference on Sensor, Mesh and Ad Hoc Communications and Networks, pp. 350–358. IEEE, Piscataway (2011)
39. Steffen, M., Džanan, S., Simon, R.D., et al.: Simbench–a benchmark dataset of electric power systems to compare innovative solutions based on power flow analysis. Energies 13(12), 3290 (2020)
40. Tjaden, T., Bergner, J., Weniger, J., et al.: Repräsentative elektrische lastprofile für einfamilienhäuser in deutschland auf 1-sekündiger datenbasis. hochschule für Technik und Wirtschaft (HTW) Berlin, Lizenz: CC-BY-NC-4.0, Heruntergeladen am 1.1.2019, Datensatz
41. Lange, I.: Temperature and solar irradiation data from the hamburg weather mast of the meteorological institute of the university of hamburg for the year 2021 (2022). Personal note on 29 March 2022

How to cite this article: Ipach, H., Fisser, L., Becker, C., Timm-Giel, A.: Distributed utility-based real-time power flow optimization in ICT-enabled low voltage distribution grids. IET Gener. Transm. Distrib. 17, 2900–2925 (2023). https://doi.org/10.1049/gtd2.12653

APPENDIX A

TABLE A1 Prosumer configurations

	Battery-electric vehicle				Photovoltaic plant			Heat Pump						
INC	$\dot{p}_{\mathrm{n}}$ **(kW)**	E_{bat} **(kWh)**	soc_{init} $(\frac{\%}{100})$	**Phase**	$\dot{p}_{\mathrm{peak}}$ **(kW)**	**Orientation (°)**	**Tilt (°)**	Q_{annual} **(kWh)**	**Sink**	**Source**	V **(L)**	$\dot{p}_{\mathrm{min,on}}$ **(kW)**	$\dot{p}_{\mathrm{max}}$ **(kW)**	ϑ_0 **(°C)**
1	3.7	40	0.523	a	9.36	43.44	53.16	29994.62	Radiator	Groundwater	1290.20	1.47	4.43	53.85
2	11	50	0.852	All	16.12	-37.43	22.96	47293.75	Radiator	Air	1715.10	3.26	5.28	49.35
3	22	70	0.712	All	7.37	101.81	39.16	54808.38	Floor	Brine	1526.58	0.33	3.07	52.69
4	22	70	0.613	All	15.42	96.93	22.49	26730.19	Floor	Brine	1324.39	1.12	3.35	45.43
5	11	50	0.812	All	17.62	13.56	55.37	28303.37	Floor	Brine	1456.98	0.33	2.20	53.12
6	11	70	0.709	All	15.91	93.89	37.83	23438.70	Radiator	Brine	1684.12	1.35	4.04	53.49
7	11	60	0.692	All	10.39	5.16	22.74	25406.87	Water	Air	1099.10	0.82	5.01	39.49
8	11	50	0.556	All	15.90	33.17	23.06	44709.98	Floor	Groundwater	1355.58	1.23	3.72	52.89
9	11	60	0.596	All	7.09	85.68	41.55	65843.22	Water	Brine	1125.00	0.64	4.32	40.95
10	3.7	40	0.630	a	9.71	3.15	23.02	39405.28	Water	Brine	1423.84	2.20	6.60	38.02
11	11	80	0.780	All	11.29	107.19	27.35	34164.03	Radiator	Air	1117.46	0.62	3.77	52.71
12	22	70	0.594	All	18.16	-36.95	37.45	37863.37	Floor	Brine	1851.36	1.12	3.35	54.39
13	11	70	0.674	All	7.31	83.87	39.91	45782.06	Water	Groundwater	1749.61	2.36	7.11	41.71
14	11	60	0.882	All	18.20	-35.81	43.33	39698.37	Water	Brine	1100.27	2.20	6.60	38.67
15	3.7	40	0.885	a	16.98	-32.60	44.82	35069.04	Water	Groundwater	1125.54	2.36	7.11	39.30
16	3.7	40	0.610	a	19.57	-44.81	34.91	28684.39	Water	Brine	1761.12	2.20	3.94	39.92
17	3.7	40	0.806	a	10.52	-26.13	44.75	41535.24	Floor	Brine	1855.84	0.33	3.07	46.50
18	11	60	0.873	All	8.07	64.50	26.29	32138.23	Water	Brine	1161.91	2.20	3.94	40.17
19	3.7	40	0.710	a	8.61	1.46	31.02	36280.62	Radiator	Groundwater	1438.52	1.47	4.43	52.28
20	22	70	0.754	All	17.42	6.32	51.95	53120.33	Water	Air	1516.39	4.33	7.03	39.31
21	11	70	0.694	All	19.48	119.16	26.12	52394.42	Radiator	Groundwater	1751.88	1.47	4.43	57.86
22	22	80	0.603	All	15.48	88.80	28.93	44128.51	Radiator	brine	1927.44	0.39	3.69	46.70
23	11	70	0.689	All	12.24	35.23	29.72	76503.04	Water	air	1408.14	0.82	5.01	38.29
24	22	80	0.809	All	9.31	-9.44	39.18	27714.77	Floor	brine	1985.70	0.33	2.20	47.96
25	22	70	0.801	All	17.51	112.02	20.03	48700.51	Radiator	groundwater	1649.27	1.47	4.43	42.07
26	11	70	0.603	All	18.08	4.75	21.21	31039.84	Water	air	1155.93	2.32	4.74	40.56
27	11	60	0.802	All	6.38	11.14	38.46	34543.62	Radiator	groundwater	1807.86	1.10	1.96	52.27
28	3.7	40	0.645	a	8.24	69.34	26.50	44904.25	Floor	groundwater	1077.63	1.23	3.72	54.27
29	22	70	0.529	All	17.48	39.38	47.18	40222.50	Radiator	air	1345.91	0.62	3.77	54.72
30	22	80	0.823	All	17.72	114.27	51.81	40553.55	Radiator	groundwater	1562.10	1.47	4.43	55.64
31	11	60	0.875	All	9.72	-31.90	43.13	42120.11	Water	groundwater	1744.75	2.36	7.11	37.56
32	3.7	40	0.537	a	9.19	3.37	47.79	41493.55	Radiator	brine	1451.43	1.35	4.04	51.02
33	22	80	0.896	All	11.46	44.62	35.64	40736.45	Radiator	air	1443.71	0.62	3.77	52.22
34	11	60	0.649	All	13.09	-40.58	21.85	21795.76	Floor	air	1912.70	0.55	3.36	42.59
35	11	60	0.859	All	6.43	72.25	37.58	56211.63	Water	brine	1279.34	2.20	6.60	39.01
36	11	50	0.762	All	17.55	21.67	34.88	38514.96	Water	brine	1717.40	0.64	6.03	37.35
37	3.7	40	0.808	a	13.02	48.54	43.88	34971.20	Floor	brine	1462.95	0.33	2.20	56.55

(Continues)

TABLE A1 (Continued)

	Battery-electric vehicle				Photovoltaic plant			Heat Pump						
INC	p_{n} **(kW)**	E_{bat} **(kWh)**	soc_{init} $(\frac{\%}{100})$	**Phase**	p_{peak} **(kW)**	**Orientation (°)**	**Tilt (°)**	Q_{annual} **(kWh)**	**Sink**	**Source**	V **(L)**	$p_{\mathrm{min,on}}$ **(kW)**	p_{max} **(kW)**	ϑ_0 **(°C)**
38	22	80	0.568	All	16.62	112.20	25.37	42331.23	Water	brine	1328.82	0.64	6.03	42.70
39	3.7	40	0.771	a	8.46	6.61	29.11	37280.08	Water	groundwater	1291.72	2.36	7.11	39.69
40	3.7	40	0.700	a	19.48	110.85	52.59	45283.08	Floor	groundwater	1561.29	1.23	3.72	46.72
41	22	70	0.630	All	16.27	94.57	30.57	40560.78	Radiator	air	1065.80	0.62	3.77	47.22
42	11	60	0.563	All	10.15	39.55	36.41	39544.08	Floor	Air	1308.64	1.55	3.18	53.04
43	11	50	0.865	All	19.23	-13.82	57.44	34562.87	Water	air	1186.29	2.32	4.74	39.75
44	22	70	0.761	All	15.51	6.70	31.02	27032.70	Water	Brine	1654.28	2.20	6.60	37.35
45	11	60	0.800	All	17.61	49.57	25.81	47879.91	Radiator	Air	1932.39	1.74	3.56	48.77
46	3.7	40	0.771	a	5.68	4.81	48.08	80919.22	Floor	Air	1824.90	0.55	3.36	42.30
47	3.7	40	0.580	a	5.83	-7.25	42.68	46308.68	Water	Groundwater	1172.97	2.36	7.11	37.13
48	11	60	0.888	All	16.14	43.48	44.46	51418.29	Radiator	Air	1509.38	3.26	5.28	42.22
49	11	80	0.660	All	9.57	40.10	21.68	40825.90	Radiator	Groundwater	1318.35	1.47	4.43	47.66
50	11	50	0.640	All	12.75	-32.55	36.69	40979.27	Water	Air	1578.05	0.82	5.01	43.82
51	22	70	0.630	All	7.34	-41.25	20.17	24522.93	Water	Brine	1888.96	0.64	6.03	43.48
52	11	50	0.839	All	19.67	-34.14	29.86	38559.04	Water	Air	1653.55	0.82	5.01	39.38
53	3.7	40	0.653	a	12.54	62.35	48.24	34372.62	Water	Groundwater	1365.50	2.36	7.11	38.37